Evaporation effect on the contact angle and contact line dynamics

Vadim Nikolayev

Evaporation effect on the contact angle and contact line dynamics

Vadim S. Nikolayev

Abstract This chapter shows how the evaporation and condensation can modify the wetting conditions. First, we review the microscopic-scale phenomena acting near the contact line: Kelvin effect, hydrodynamic slip, vapor recoil, surface forces, and interfacial resistance. Then we address the theory of liquid flow in the wedge under evaporation at partial wetting conditions, more common in practice than complete wetting. The importance of the correct formulation of the boundary conditions at the contact line is shown. Two main evaporation regimes are addressed next. First, the evaporation into pure vapor atmosphere is considered (like in bubble growth in boiling). It is controlled by the flow in the liquid. In the presence of contact line receding, this problem is solved by asymptotic matching of the three liquid regions: (i) the microregion near the contact line controlled by the phenomena described above, (ii) the intermediate region where the surface tension competes with the viscous effects (iii) macroregion controlled by the liquid bulk effects. The asymptotic matching results in an expression for the apparent contact angle that depends both on the evaporation rate and on the contact line velocity. From such an analysis, the contact line receding dynamics caused by evaporation can be found. The theory is then compared to the available experimental data. Finally, we consider another regime of the wedge evaporation, that in the atmosphere of the neutral gas, controlled by the vapor diffusion in the diffusion boundary layer. As the evaporation is weaker in this case, its effect on the apparent contact angle is smaller. However we show how it depends on the key parameters of evaporation, like e.g. the boundary layer thickness.

Key words: partial wetting, evaporation, diffusion, Kelvin effect, contact line dynamics

Université Paris-Saclay, CEA, CNRS, SPEC, 91191, Gif-sur-Yvette, France,
e-mail: vadim.nikolayev@cea.fr

Contents

1 Introduction

Evaporation and condensation phenomena are met widely both in everyday life and in various industrial processes. The some evident everyday examples are the water boiling in one's kitchen, linen drying on open air or the morning dew disappearance on the windshield of a car. As industrial examples, one can list the steam generation for turbines used in power plants and the two-phase cooling of micro-processors with heat pipes used now in every laptop computer and mobile phone. One can recall also the spray cooling in high-power heat exchangers or the drying of solvent during thin film coating based on the colloidal solutions. In all these cases, a solid surface in contact with the liquid can be partially dried so triple liquid-gas-solid contact lines appear.

The experimental studies of evaporation effect on the wetting are difficult and thus quite rare; for this reason this chapter is mainly theoretical. Some experimental data are however discussed in sec. 2.5 below.

The contact line problem is a particular case of the free-interface problem, which can be theoretically considered thanks to the Laplace equation

$$\Delta p = K\sigma \tag{1}$$

that defines the local interfacial pressure jump

$$p_V - p_L = \Delta p, \tag{2}$$

in terms of the surface tension σ and its curvature K; the pressures at the interface on both sides of it are denoted p_V (vapor) and p_L (liquid).

Note that the physical phenomena presented in this chapter remain invariant with respect to the sign of the mass exchange so the presentation below applies to the condensation case as well.

The mass exchange rate is always limited by the slowest dynamic phenomenon. For this reason, the physics of evaporation differs depending on the gas composition. One can consider two limit cases. In the first, the gas is air (or another non-condensible gas) with a relatively small vapor density. This is a case of drying on open air in the absence of substrate heating. The slowest dynamic phenomenon is the vapor diffusion necessary to evacuate the vapor from the gas-liquid interface to the gas bulk. The diffusion occurs in a boundary layer that forms near the interface. Farther away, the convection takes over.

In the second case, the gas is a pure vapor of the evaporating liquid and the evaporation occurs because of the substrate heating. The diffusion is not relevant here and the evaporation is limited only by the heat supply rate. Evidently, the mass exchange is much stronger in the second case. This is the case e.g. of bubble growth in boiling.

In a tiny vicinity of the contact line called microregion hereafter, the liquid forms a curved wedge. Such a geometric singularity causes a strong increase of evaporation in the microregion, which is one of the motivation for the studies of the contact lines

in presence of phase change. There is another, perhaps even more important reason for the interest to the microregion. As will be discussed in sec. 1.1, the singularity of the mass transfer causes a strong curvature that leads to a large apparent contact angle (i.e. the slope of the gas-liquid interface at a macroscopically measurable scale). In other words, evaporation can lead to a non-negligible change in wetting conditions. This change is ruled out by effects that act at the microscopic scale. The objective of this chapter is to show how this apparent angle can be determined theoretically and to analyze its dependence on the system parameters.

The two-dimensional geometry is considered below. This is justified by a much stronger curvature of the gas-liquid interface in the plane perpendicular to the solid than in the plane parallel to the solid.

This chapter is structured as follows. In the following sections we consider the microscopic phenomena that are important in the microregion but negligible on the macroscopic scale. Next, we address two limit cases of evaporation: first, the evaporation to the pure vapor and next, the isothermal liquid drying the open air or another gas. But first of all, we give a qualitative picture explaining the evaporation impact on the contact angle.

1.1 How evaporation can modify the wetting conditions?

First of all one should mention that the evaporation cannot influence the static contact angle because it is provided by the balance of intermolecular forces that are in most cases attractive and thus tend to prevent evaporation (see Potash and Wayner [45] for an extended discussion). Evaporation can only impact the apparent contact angle, i.e. that observed macroscopically. To understand this impact, let us begin with a qualitative consideration of the microregion. There are two physical reasons for the difference between the apparent and microscopic contact angles. Both reasons are linked to the strong evaporation in the microregion. The first is related to the viscous pressure drop caused by the hydrodynamic flow. The second is the vapor recoil effect. We discuss here only flow-induced apparent contact angle. The vapor recoil will be discussed in sec. 1.2.4.

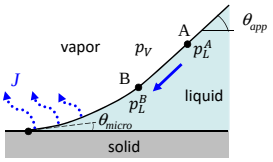

Fig. 1 Liquid wedge at evaporation. The fluid flow is shown by the blue arrows.

Consider two points A and B on the vapor-liquid interface of the wedge at evaporation, with the point B closer to the contact line than the point A (Fig. 1). Evaporation is the strongest in the contact line vicinity so there is a liquid flow toward

the contact line to replenish the liquid loss. Because of the viscosity, a pressure drop appears, so there is a difference between the liquid pressures at the points A and B:

$$p_L^A > p_L^B.$$

On the other hand, the vapor flow is much quicker, so the vapor pressures at the vapor side of the interface are both equal to p_V. From Eqs. (1-2), one concludes that $K^B > K^A$, so the interfacial curvature grows toward the contact line. Note that the curvature is a rate of change of the interface slope along the interface (it is its geometrical definition). This means that the slope varies sharply near the contact line, which can cause a strong difference between the microscopic contact angle θ_{micro} and the macroscopic (apparent) contact angle θ_{app}. This effect has first been discovered by Wayner et al. [58] and studied by many other researchers. Initially, it was however incorrectly attributed to the impact of the surface forces discussed in sec. 1.2.3.

1.2 Relevant microscopic phenomena

Evidently, near the contact line, the distance between the liquid-vapor interface and the solid is very small. This is why several effects otherwise completely negligible, become important in this region.

1.2.1 Hydrodynamic slip

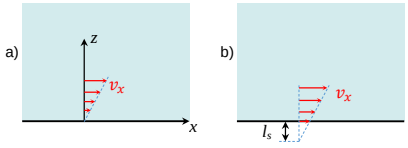

Fig. 2 Variation of the tangential component of the liquid velocity in the close vicinity of the solid in case of the (a) no-slip boundary condition and (b) in case of slip. The slip length definition is shown.

For a hydrodynamic problem, one needs to define the boundary conditions, in particular on the solid surface. One evident condition is the non-penetration of the liquid into the solid. The normal to the surface component of the liquid velocity v_z is thus zero (cf. Fig. 2a for the reference system). Usually one considers that the liquid molecules stick to the solid so the tangential to the surface component v_x of the liquid velocity is zero on it, which is referred as the no-slip condition (Fig. 2a). When the surface is non-wettable, the statistical physics of liquids [21] shows that the

liquid can slide along the solid when the tangential hydrodynamic stress is large. This phenomenon is characterized by the slip length l_s defined with the Navier boundary condition (Fig. 2b)

$$v_x = l_s \frac{\partial v_x}{\partial z}. \tag{3}$$

One needs to mention that the slip of liquid along the solid substrate is well confirmed experimentally [43], and measurements permit to determine the slip length within 10 nm accuracy [6]. The slip length can also be obtained with the molecular dynamic simulations. More detailed discussion on this phenomenon may be found in the review articles [30, 32]. The characteristic value of l_s is of the order of 20 nm. The slip effect is expected to be important at a distance $\ell_s \sim l_s/\theta_{micro}$ from the CL where θ_{micro} is a contact angle assumed to be small here. It is in the denominator because the slip length is measured on the z axis. For small θ_{micro}, $\ell_s \gg l_s$.

1.2.2 Kelvin effect

The Kelvin effect, sometimes called the Gibbs-Thomson effect [31], provides a dependence of the local temperature T_i of the vapor-liquid interface on the local interfacial pressure jump Δp that, apart from the interface curvature (cf. Eq. 1) can depend on several other factors discussed in the next sections. Consider a portion of the liquid-vapor interface that may globally be out of equilibrium. The portion is however assumed to be at *local* equilibrium, so the following equality holds for the chemical potentials of the phases:

$$\mu_V(p_V, T^i) = \mu_L(p_L, T^i) \tag{4}$$

A similar expression can be written for a flat liquid-vapor interface at equilibrium at the temperature T^i, where both liquid and vapor pressures are equal to $p_0 = p_{sat}(T_i)$:

$$\mu_V(p_0, T^i) = \mu_L(p_0, T^i). \tag{5}$$

Let us develop now both sides of Eq. (4) into the Taylor series around p_0 by using the thermodynamic relation

$$\left(\frac{\partial \mu}{\partial p}\right)_T = \frac{1}{\rho},$$

where ρ is the density. With the help of Eq. (5), one readily obtains

$$\frac{p_V - p_0}{\rho_V} = \frac{p_L - p_0}{\rho_L}. \tag{6}$$

By using Eqs. (2, 6), one gets

$$p_V = p_0 - \Delta p \frac{\rho_V}{\rho_L - \rho_V}. \tag{7}$$

In what follows, we assume the smallness of the difference $|p_V - p_0| \ll p_0$.

For the pure vapor case, one can make use of the Clausius-Clapeyron equation

$$\left.\frac{dp}{dT}\right|_{sat} = \frac{\mathcal{L}\rho_L\rho_V}{T_{sat}(\rho_L - \rho_V)}, \tag{8}$$

where $\mathcal{L}$ is the latent heat and $T_{sat} = T_{sat}(p_V)$. With the relations

$$\left.\frac{dp}{dT}\right|_{sat} = \frac{p_0 - p_V}{T^i - T_{sat}}$$

and (7), one gets the final expression for the local equilibrium interface temperature as a function of pressure jump

$$T^i = T_{sat}\left(1 + \frac{\Delta p}{\mathcal{L}\rho_L}\right). \tag{9}$$

For the evaporation into the open air, one can use the ideal gas equation for the vapor:

$$p_V = \rho_V^i \frac{R_g T}{M}, \tag{10}$$

$$p_0 = \rho_0 \frac{R_g T}{M}, \tag{11}$$

where ρ_0 is the saturation vapor density in the air over the flat interface at equilibrium, R_g is the gas constant and M, vapor molar weight. By using these expressions in Eq. (7), one finally obtains the local equilibrium interfacial vapor density ρ_V^i as a function of pressure jump under the assumption $\rho_V^i \ll \rho_L$:

$$\rho_V^i = \rho_0 - \Delta p \frac{M\rho_0}{\rho_L R_g T}, \tag{12}$$

Note that only local (and not global) equilibrium hypothesis was used. This means that the quantities T^i, ρ_V^i are allowed to vary along the interface while following the variation of Δp.

1.2.3 Surface forces

Consider a thin liquid film of a homogeneous thickness h on a solid substrate at equilibrium (Fig. 3). The liquid is surrounded by its vapor and the system is at the saturation temperature T_{sat} given by the bulk vapor pressure. The excess free energy W (appearing due to the interaction of interfaces) per unit area is

$$W(h) = \sigma_{SL} + \sigma + P(h), \tag{13}$$

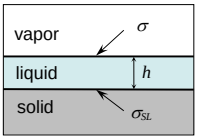

Fig. 3 Thin liquid film on a solid substrate.

where the first two terms in the right side are the tensions of the solid-liquid and vapor-liquid interfaces, respectively. The term $P(h)$ is the energy of the surface (or thin film) forces [22] that appear because of the molecules of the solid "feel" the vapor-liquid interface. It is a differential contribution (proportional to the difference of liquid and vapor densities) of the interactions of the liquid and vapor molecules with those of the solid. Evidently, the h scale at which $P(h)$ matters is defined by the range of intermolecular interaction. Usually, this distance does not exceed several tens of nm. Obviously, $P(h \to \infty) = 0$.

The limit $h \to 0$ may be attained at partial wetting. It is evident that $W(h \to 0)$ has to be finite in this case. It has been postulated by [8] that

$$W(h \to 0) = \sigma_{SG}, \tag{14}$$

which corresponds to the energy of the dry (bare) solid-gas interface. Equations (13,14) then lead to the constraint $P(h \to 0) = S$, where

$$S = \sigma_{SG} - \sigma_{SL} - \sigma \tag{15}$$

is the spreading coefficient. A more general case [59, 60] $P(h \to 0) \geq S$ is adopted here. The inequality can be justified by the existence of a monolayer of fluid molecules that may modify the surface energy so $W(h \to 0) > \sigma_{SG}$.

With the account of the surface forces, the Laplace equation (1) becomes

$$\Delta p = K\sigma + \Pi(h), \tag{16}$$

where Π is called the disjoining pressure related to P via

$$\Pi = -\frac{\partial P}{\partial h}. \tag{17}$$

In general, the disjoining pressure includes contributions from dispersion, electrical double layers, electrostatic and structural forces [22]. Within a conventional for the contact line problem approach suggested by Wayner et al. [45], only the dispersion component (neglecting the retardation effect) is accounted for. This is justified for $h \gtrsim 10$ nm,

$$\Pi(h) = A/(6\pi h^3). \tag{18}$$

The Hamaker constant A is positive for conventional couples of solid surfaces and fluids. For the "high-energy" metal or oxidized surfaces, its value is $A \sim 10^{-20} - 10^{-19}$ J.

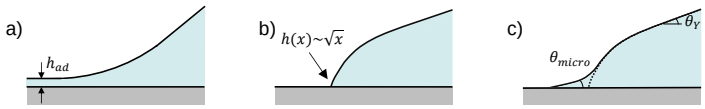

Fig. 4 Wedge shape in the microregion: (a) for the complete wetting; (b) for complete wetting and strong evaporation (with the dried wetting film); the interface shape is defined by the de Gennes solution; (c) for the partial wetting.

Because of singularity of Eq. (18) at $h \to 0$, such a Π dependence results in a configuration where the solid is covered with a continuous (wetting or adsorption) film, generally of nanometric thickness h_{ad} so the vapor contact with the bare solid is nonexistent. Such a situation corresponds to the complete wetting case. When a liquid wedge configuration is forced by the macroscopic liquid shape, the wedge ends by the film (Fig. 4a). Another solution [17], where the contact line exists even for the complete wetting case, prevails when the evaporation rate is higher than a threshold [48] so the film dries out (Fig. 4b) and $h(x) \sim \sqrt{x}$ near the contact line $x = 0$.

At equilibrium, the wedge geometry appears at partial wetting (Fig. 4c), where $S < 0$. At a distance from the contact line, where the surface forces vanish (where $h \lesssim 100$ nm), the meniscus slope is θ_Y defined by the Young formula $\cos\theta_Y = 1 + S/\sigma$. At a smaller scale ($h \sim 1$ nm), the meniscus forms a contact angle θ_{micro} linked to θ_Y via the expression [60]

$$\cos\theta_{micro} = 1 + \frac{S - P(h \to 0)}{\sigma} = \cos\theta_Y - \frac{P(h \to 0)}{\sigma}. \tag{19}$$

Note that the assumption (14) results in $\theta_{micro} = 0$; a more general case is considered here.

To describe the partial wetting configuration at equilibrium, the disjoining pressure must be regularized at small h, e.g. [26]:

$$\Pi(h) = \begin{cases} C_1 h + C_2, & h \in (0, h_m) \\ A/(6\pi h^3), & h \in (h_m, \infty) \end{cases} \tag{20}$$

Indeed, $\Pi(h)$ needs to be integrable at $h \to 0$; $P(h)$ would be infinite otherwise. The constant h_m is of the order of several nm and defines the position of the maximum of the $\Pi(h)$ function; $C_{1,2}$ are the constants defined from the continuity of $\Pi(h)$ at $h = h_m$ as

$$C_1 = (A - 4\pi h_m^2 P(h \to 0)/(2\pi h_m^4),$$
$$C_2 = (6h_m^2 \pi P(h \to 0) - A)/(3\pi h_m^3),$$

where $P(h \to 0)$ can be determined from θ_{micro} and θ_Y via Eq. (19).

At $h \geq h_m$ but still in the contact line vicinity, the interface follows the $\sqrt{x}$ law, which cross-overs to the straight wedge shapes both at $h < h_m$ and at larger h

(Fig. 4c) but of different slopes. The slope near the contact line is θ_{micro}. Farther away, it is equal to θ_Y at equilibrium (cf. Eq. 19) and is different from it when the phase change occurs.

The above approach has been developed in the "local" approximation, where P is assumed to be independent of the spatial variation of h (i.e., on its spatial derivatives). A more adequate but also more complicated non-local approach [51] (where P is considered to be a functional of $h(x)$) gives a correction to (19) at large θ_Y. In particular, $\theta_{micro} \neq 0$ even for $P(h \to 0) = S$. For small angles, the results of the local and non-local approaches are essentially the same.

1.2.4 Vapor recoil

Let us consider now a portion of the liquid-vapor interface of area A at evaporation conditions, see Fig. 5a. Every fluid molecule evaporated from the liquid interface causes a recoil force analogous to that created by the gas emitted by a rocket engine. It pushes the interface towards the liquid side in the normal direction. This force appears because the fluid necessarily expands while transforming from liquid to gas phase. Obviously, the stronger the evaporation rate, the larger is the vapor recoil force.

During the time $\mathrm{d}t$, the fluid mass $\mathrm{d}m_V$ changes state from liquid to vapor. This mass can be expressed as

$$\mathrm{d}m_V = \rho_V \mathrm{d}V_V = -\rho_L \mathrm{d}V_L, \tag{21}$$

where $\mathrm{d}V_L(\mathrm{d}V_V)$ is the volume change of the liquid (vapor). As a consequence, the interface displacement is $\mathrm{d}\mathbf{l} = -\mathbf{n}\mathrm{d}V_L/A$, where $\mathbf{n}$ is the unit vector normal to the interface and directed into the liquid.

The conservation of momentum for the control volume shown in Fig. 5a reads

$$(\mathbf{v}_V + \mathbf{v}^i)\mathrm{d}m_V + \mathbf{p}_r \mathrm{d}t A = 0, \tag{22}$$

where $\mathbf{p}_r$ is the vapor recoil force per unit area, $\mathbf{v}^i = \mathrm{d}\mathbf{l}/\mathrm{d}t$ is the velocity of interface and $\mathbf{v}_V = -\mathbf{n}\mathrm{d}V_V/(A\mathrm{d}t)$ is the velocity of vapor with respect to the interface. By using this expression together with Eq. (21), the equation (22) can be rewritten as

$$\mathbf{p}_r = \mathbf{n}J^2\left(\frac{1}{\rho_V} - \frac{1}{\rho_L}\right), \tag{23}$$

where

$$J = \frac{1}{A}\frac{\mathrm{d}m_V}{\mathrm{d}t} \tag{24}$$

is the mass evaporation flux. Note that $\mathbf{p}_r$ is directed towards the liquid both for evaporation ($J > 0$) and condensation ($J < 0$) cases. The vapor recoil pressure enters the pressure balance equation as [38]

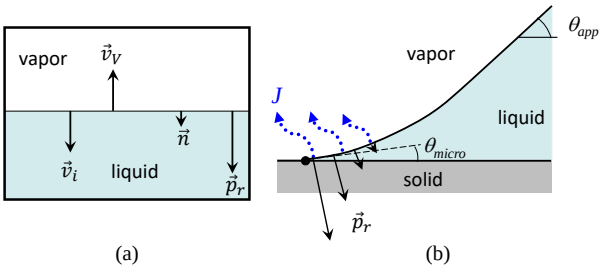

Fig. 5 (a) Vapor recoil force. (b) Effect of the vapor recoil on the apparent contact angle.

$$K\sigma = \Delta p + p_r, \tag{25}$$

where $p_r = |\mathbf{p}_r|$. In addition to the Kelvin term (9), a vapor recoil term appears in the interface temperature expression [4]

$$T^i = T_{sat}\left[\left(1 + \frac{\Delta p}{\mathcal{L}\rho_L}\right) + \frac{J^2}{2\mathcal{L}}\left(\frac{1}{\rho_V^2} - \frac{1}{\rho_L^2}\right)\right]. \tag{26}$$

The vapor recoil effect causes an increase of the apparent contact angle just like the viscous pressure drop discussed in sec. 1.1. Indeed, the vapor recoil is the largest near the contact line (where J is very large, cf. Fig. 5b). As the curvature K is proportional to p_r according to Eq. (25), the slope changes strongly in the contact line vicinity [38], which causes a difference between θ_{app} and θ_{micro}, just like in the pressure-drop-caused effect described in sec. 1.1. The relative contribution of this effect is especially strong near the liquid-vapor critical point [39], where it causes the boiling crisis: the apparent contact angle growth induces the growth of dry area under the bubbles, which in its turn triggers the complete heater dewetting.

1.2.5 Interfacial kinetic resistance

Up to now we considered the interface at a local equilibrium. This assumption holds when phase change rates are smaller than some generally quite high value. Even for moderate average evaporation rates, high local evaporation rates can be attained in the contact line vicinity.

The non-equilibrium effects can be analyzed with the Schrage molecular-kinetic theory of evaporation [9] by using the ideal gas assumption for the vapor. According to this theory, the statistical distribution of the velocities of molecules is the Maxwell distribution. If the average vapor velocity is zero and the vapor is at temperature T_V, the mass flux perpendicular to a plane is

$$p_V\sqrt{\frac{M}{2\pi R_g T_V}}.$$

When the vapor flows with a velocity v_V perpendicularly to a plane, it is evident that the mass fluxes J^+ along $\mathbf{v}_V$ and J^- against to $\mathbf{v}_V$ should differ and depend on v_V because the velocity distribution becomes asymmetric. The expressions for them read

$$J^+ = \Gamma(a) p_V \sqrt{\frac{M}{2\pi R_g T_V}}, \tag{27}$$

$$J^- = \Gamma(-a) p_V \sqrt{\frac{M}{2\pi R_g T_V}}, \tag{28}$$

where

$$\Gamma(a) = \exp(-a^2) + a\sqrt{\pi}[1 + \mathrm{erf}(a)] \simeq 1 + a\sqrt{\pi}$$

for a small

$$a = \frac{v_V}{\sqrt{2R_g T_V / M}} = \frac{J}{p_V}\sqrt{\frac{R_g T_V}{2M}}.$$

The latter equality is obtained by using the vapor mass flux expression $J = v_V \rho_V$ and the ideal gas equation.

Consider now the liquid-vapor interface at evaporation. It is assumed that a part of molecules that come to the interface can be reflected by it so the actual incoming flux arriving back to the liquid is smaller than J^-

$$J_L = f J^- = f\Gamma(-a) p_V \sqrt{\frac{M}{2\pi R_g T_V}}, \tag{29}$$

where f is called the evaporation coefficient. At equilibrium ($J = 0$), the incoming flux would be equal to the outgoing flux

$$J_V = f p_0 \sqrt{\frac{M}{2\pi R_g T^i}}. \tag{30}$$

The case $J > 0$ differs from the case $J = 0$ only by a smaller value of J_L (given by Eq. 29) while J_V remains to be given by Eq. (30). Evidently, $T^i = T_{sat}(p_0)$. By writing $J = J_L + J_V$ one obtains

$$J = \frac{2f}{2 - f}\sqrt{\frac{M}{2\pi R_g}}\left(\frac{p_0}{\sqrt{T^i}} - \frac{p_V}{\sqrt{T_V}}\right). \tag{31}$$

The temperature is assumed to be continuous ($T^i = T_V$) so the small interfacial temperature jump [16] that may exist in some particular cases (like strong evaporation into vacuum) is neglected so Eq. (31) becomes finally

$$J = \frac{2f}{2-f}\sqrt{\frac{M}{2\pi R_g T^i}}(p_0 - p_V). \tag{32}$$

For the (isothermal) evaporation into the open air, one can again use Eqs. (10-11) to obtain

$$\rho_V^i = \rho_0 - JR_{diff}^i, \tag{33}$$

where ρ_V^i is the interfacial vapor density; R_{diff}^i is called the interfacial kinetic resistance and is defined as

$$R_{diff}^i = \frac{2-f}{2f}\sqrt{\frac{2\pi M}{R_g T_{sat}}}. \tag{34}$$

The value of evaporation coefficient can be set to unity which is verified experimentally [33].

For the pure vapor case, thanks to Eq. (8), one can linearize Eq. (32) by writing

$$p_0 - p_V = \frac{\mathcal{L}\rho_L\rho_V}{T_{sat}(\rho_L - \rho_V)}(T^i - T_{sat}),$$

that results in the expression

$$T^i = T_{sat} + R^i J\mathcal{L}, \tag{35}$$

where R^i is the interfacial thermal resistance:

$$R^i = \frac{2-f}{2f}\frac{T_{sat}\sqrt{2\pi R_g T_{sat}/M}(\rho_L - \rho_V)}{\mathcal{L}^2\rho_L\rho_V}. \tag{36}$$

By combining the above expression with Eq. (26), one can write the final expression for the local temperature of the vapor-liquid interface

$$T^i = T_{sat}\left[\left(1 + \frac{\Delta p}{\mathcal{L}\rho_L}\right) + \frac{J^2}{2\mathcal{L}}\left(\frac{1}{\rho_V^2} - \frac{1}{\rho_L^2}\right)\right] + R^i J\mathcal{L}. \tag{37}$$

as a function of Δp and J that can also vary along the interface.

One should note that R^i is typically is a tiny quantity so its effect is notable only at extremely high heat fluxes that can occur in the microregion.

1.3 Liquid flow in the wedge

The full Navier-Stokes equations in a wedge with a free curved boundary (i.e. the gas-liquid interface) are quite complex to solve. In particular, no analytical approach is possible in a general case so the only possible approach is numerical.

However the numerical algorithms describing such a problem are still insufficiently developed. The rare existing studies [1, 55] concern mainly the moving contact line problem with no phase change. Fortunately, there is a powerful tool for such studies: the lubrication approximation developed independently by Petroff [40] and Reynolds [50] to study the thin film hydrodynamics. It is based on the smallness of the Reynolds number (because of the small film thickness). The inertial terms in the Navier-Stokes equations are thus unimportant and the hydrodynamics can be described by the Stokes equations in 3D,

$$\begin{aligned} \nabla p_L &= \Delta \mathbf{v}, \\ \nabla \cdot \mathbf{v} &= 0, \end{aligned} \tag{38}$$

where $\mathbf{v}$ is the liquid velocity and $\nabla = (\partial/\partial x, \partial/\partial y, \partial/\partial z)$ is the 3D differential operator. As described in the following sections, these equations can be further simplified by considering the liquid layer in the thin film approximation.

Note the essential role of the viscosity in the contact line region (sec. 1.1). For this reason, the theoretical approaches based on the inviscid flow approximation are not relevant and will not be considered here.

In general, the contact line problem should be considered as transient: evaporation causes the progressive drying of the substrate. However a stationary regime where the contact line is pinned by a defect on the solid is equally possible: the liquid is supplied to the microregion from the liquid bulk to compensate exactly the evaporation losses.

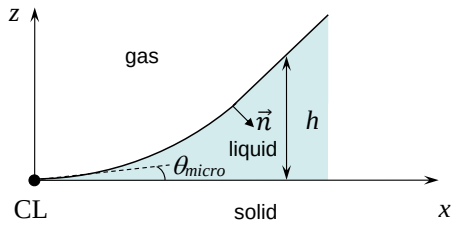

Fig. 6 Geometry of the general contact line problem. The chosen direction of the normal to the interface is shown.

To consider the apparent contact angle, a 2D geometry in the $x - z$ plane (Fig. 6) is sufficient. For thin fluid layers, the fluid is supposed to move mainly along x axis, i.e. $v_x \gg v_z$, where $\mathbf{v} = (v_x, 0, v_z)$. In addition, the v_x variation across the layer is assumed to be much larger than along it: $\partial v_x/\partial z \gg \partial v_x/\partial x$. The Stokes equations then reduce to:

$$\frac{\partial p_L}{\partial x} = \mu \frac{\partial^2 v_x}{\partial z^2}, \tag{39}$$

$$\frac{\partial p_L}{\partial z} = 0. \tag{40}$$

By taking the z derivative of (39) and using (40) one arrives at the equation $\partial^3 v_x/\partial z^3 = 0$, the solution of which is

$$v_x = C_1 + C_2 z + C_3 z^2, \tag{41}$$

where $C_{1,2,3}$ are independent of z. They are to be determined from the boundary conditions. The first of them defines the tangential stress at the free vapor-liquid interface $z = h(x)$ to be equal to the surface tension gradient induced (Marangoni) stress

$$\mu \frac{\partial v_x}{\partial z} = \frac{\partial \sigma}{\partial x}. \tag{42}$$

The volume flux Φ flowing through the film at a given position x

$$\Phi = \int_0^h v_x(z) \mathrm{d}z \tag{43}$$

serves as the second equation. The third condition is given by Eq. (3). The back substitution of the solution into Eq. (39) written at the vapor-liquid interface results in

$$\mu\Phi = \frac{\partial \sigma}{\partial x}\left(\frac{h^2}{2} + h l_s\right) + \left(\frac{h^3}{3} + h^2 l_s\right)\frac{\partial \Delta p}{\partial x}, \tag{44}$$

where the equality $\partial \Delta p/\partial x = -\partial p_L/\partial x$ has been used. It assumes the constant gas pressure which can be justified by the small gas viscosity and density with respect to those of the liquid, so the gas pressure gradient is much smaller.

By using the fluid mass conservation, Φ can also be expressed via the component $v_n = \mathbf{v} \cdot \mathbf{n}$ of the liquid velocity normal to the vapor-liquid interface (positive when directed along $\mathbf{n}$, see Fig. 6):

$$\Phi \simeq \int_{x_{CL}}^{x} v_n(x) \mathrm{d}x. \tag{45}$$

Eq. (45) can thus be rewritten as

$$v_n = \frac{\partial \Phi}{\partial x}, \tag{46}$$

where v_n is related to the evaporation flux J (24) at the interface via the mass conservation law

$$J = (v^i - v_n)\rho_L. \tag{47}$$

The normal interface velocity

$$v^i = -\frac{\partial h}{\partial t}\left[1 + \left(\frac{\partial h}{\partial x}\right)^2\right]^{-1/2} \simeq -\frac{\partial h}{\partial t}, \tag{48}$$

is considered to be positive if directed inside the liquid (as the vector $\mathbf{n}$ in Fig. 6). Here the small slope approximation is applied.

By injecting (44,47), and (48) into (46), one arrives finally at the expression [37]

$$\frac{\partial}{\partial x}\left[h\left(\frac{h}{2}+l_s\right)\frac{\partial\sigma}{\partial x}+h^2\left(\frac{h}{3}+l_s\right)\frac{\partial\Delta p}{\partial x}\right]=-\mu\left(\frac{\partial h}{\partial t}+\frac{J}{\rho_L}\right). \tag{49}$$

In the same, small slope approximation, the curvature

$$K=\frac{\partial^2 h}{\partial x^2}\left[1+\left(\frac{\partial h}{\partial x}\right)^2\right]^{-3/2} \tag{50}$$

can be approximated as $K\simeq\partial^2 h/\partial x^2$, and Eq. (25) reduces to

$$\sigma\frac{\partial^2 h}{\partial x^2}=\Delta p+p_r. \tag{51}$$

If both the slip, Marangoni and vapor recoil effects are neglected, Eq. (49) takes a simpler form

$$\sigma\frac{\partial}{\partial x}\left(\frac{h^3}{3}\frac{\partial^3 h}{\partial x^3}\right)=-\mu\left(\frac{\partial h}{\partial t}+\frac{J}{\rho_L}\right). \tag{52}$$

The theory can be generalized to the 3D case by writing

$$\sigma\nabla\cdot\left[\frac{h^3}{3}\nabla(\nabla^2 h)\right]=-\mu\left(\frac{\partial h}{\partial t}+\frac{J}{\rho_L}\right), \tag{53}$$

where $\nabla=(\partial/\partial x,\partial/\partial y)$ is the 2D differential operator and $h=h(x,y,t)$.

One can distinguish several cases related to the CL motion. When the wedge is immobile and stationary, $\partial h/\partial t=0$. On the other hand, the CL motion is convenient to consider in the reference where CL is immobile, in which, instead of the $\partial h/\partial t$ term, one has

$$\frac{\partial h}{\partial t}-v_{CL}\frac{\partial h}{\partial x}, \tag{54}$$

where the CL velocity v_{CL} is assumed to be positive at liquid receding. The $\partial h/\partial t$ term describes now only the slope change. For a large liquid volume, this term is much smaller with respect to the second, at least in the CL vicinity. This is why in the next section it is neglected.

1.4 Boundary conditions

Eq. (49) is the fourth order differential equation. To solve it, one needs four boundary conditions. In the partial wetting case considered here, two of them are geometrical constraints defined at the CL,

$$\begin{aligned} h(x \to 0) &= 0, \\ \partial h/\partial x|_{x\to 0} &= \theta_{micro}. \end{aligned} \tag{55}$$

They are sufficient to describe the macroscopic liquid shape. However in the microscopic and intermediate regions (i.e. for the wedge geometry) other conditions need to be imposed. The third boundary condition is given by the matching of the pressure to its macroregion value, i.e. at $x \to \infty$. The interfacial pressure jump in macroregion is expected to be much smaller than in other regions because of much smaller K and J. For this reason, the condition

$$\Delta p(x \to \infty) = 0 \tag{56}$$

is applied.

The fourth boundary condition is not straightforward. It comes form the regularity of all the variables at the contact line. Indeed, from the physical point of view, the measurable quantities cannot be infinite. It can be proven mathematically (cf. the online supplementary material to the work of Janeček et al. [28]) that a regular solution indeed exists for the case of the pure vapor.

The fourth boundary condition is specific to each mode of evaporation. However some general features can be determined, in particular the J asymptotics. We start from Eq. (49), in which $\partial h/\partial t$ is replaced by $-v_{CL}\partial h/\partial x$ as discussed in sec. 1.3. To comply to the evaporation in the open air with no substrate heating, the Marangoni term is omitted for this derivation (a more complete derivation can be found in sec. 2.1 below). One can integrate Eq. (49) (with the substitution of from 0 to x and tend x to 0 by assuming the finiteness of $J(x \to 0)$. One readily obtains

$$x\frac{\partial \Delta p}{\partial x} = \frac{\mu}{l_s \theta_{micro}}\left[v_{CL} - \frac{J}{\rho_L \theta_{micro}}\right]. \tag{57}$$

If the pressure does not diverge at CL (i.e. Δp saturates at $x \to 0$), the left hand side is zero, so

$$J(x \to 0) = \theta_{micro}\rho_L v_{CL}. \tag{58}$$

In the important particular case of immobile contact line, $J(x \to 0) = 0$.

Eq. (58) shows that a regular solution can be obtained at the contact line, in spite of the no-slip boundary condition imposed at the solid-liquid interface: at the microscopic scale, the interface advances ($v_{CL} < 0$) by the curvature driven condensation ($J < 0$) or recedes ($v_{CL} > 0$) by evaporation ($J > 0$). Eq. (58) is easy to interpret: in the reference of the fluid wedge, the whole amount of the fluid flow created by the entrainment by the moving substrate is spent as a mass exchange at the liquid-vapor interface.

Consider now the case of the isothermal CL motion with no overall mass exchange. When the contact line advances ($v_{CL} < 0$), the mass flux at the CL is negative so condensation occurs in the vicinity of the CL. It means that $J(s)$ should change sign farther away from the CL so evaporation occurs there. It should exactly compensate the condensed mass. A possibility of such an effect was already discussed by Pomeau

[44], Reyes and Wayner [49]. Such an effect is discussed in detail by Janeček et al. [29].

As the fourth boundary condition, one can use the finiteness of pressure at the CL. Eq. (57) suggests a form [25, 37]

$$x\frac{\partial \Delta p}{\partial x}\bigg|_{x\to 0} = 0. \tag{59}$$

Note the role of the Kelvin effect that is responsible for the explicit form of the fourth boundary condition. If the Kelvin effect is neglected, the pressure jump at the contact line cannot be identified explicitly thus forcing application of asymptotic methods of solution instead of a generally simpler numerical treatment. The finiteness of pressure and of evaporation flux clearly shows that the Kelvin effect alone is sufficient to regularize all the physical quantities at the contact line.

2 Evaporation into pure vapor

Now that all the basic "bricks" of the microscale phenomena are explained, one can consider two most important regimes of evaporation listed in sec. 1. First, the evaporation of liquid into the atmosphere of its pure vapor is discussed. It is the important case met in numerous industrial applications oriented to cooling, like growth of bubbles in boiling, heat pipes, and sessile drop evaporation during the spray cooling.

Near the contact line, the interfacial temperature T^i can vary along the interface according to Eq. (37), so the Marangoni stress

$$\frac{\partial \sigma}{\partial x} = -\gamma \frac{\partial T^i}{\partial x}, \tag{60}$$

can be important. Here $\gamma = -\mathrm{d}\sigma/\mathrm{d}T$ is positive for pure fluids.

A large amount of work has been done by many researchers to understand this regime. One can cite the works by Anderson and Davis [2], Hocking [19], Moosman and Homsy [34], Morris [35], Potash and Wayner [45], Rednikov and Colinet [48], Stephan and Hammer [54] as the main milestones.

Since the vapor heat conductivity is much smaller than that of the liquid, the heat flux into the vapor can be neglected, and the interfacial energy balance reads

$$q_L^i = \mathcal{L}J. \tag{61}$$

One can see now that, in this regime, the mass evaporation flux is completely defined by the heat transfer in the liquid: the liquid heat flux is spent to compensate the latent heat of vaporization.

Similarly to the above hydrodynamics approach, one can use the thin film approximation to simplify the heat transfer problem in the contact line vicinity. First,

the thermal inertia of the thin film is small and can be neglected so the problem to solve is stationary. Second, the heat convection can be neglected at small scales with respect to the heat conduction, so the temperature distribution in the liquid obeys the equation

$$\nabla^2 T_L = 0. \tag{62}$$

The boundary conditions are the fixed temperature both on the solid (where the superheating ΔT is fixed) and on the free interface:

$$\begin{aligned} T_L(z=0) &= T_{sat} + \Delta T, \\ T_L(z=h) &= T^i. \end{aligned} \tag{63}$$

One can use the small-slope approximation to solve this problem. The solution that satisfies the boundary conditions (63) results in the heat flux

$$q_L^i = k_L \frac{T_{sat} + \Delta T - T^i}{h}. \tag{64}$$

at the free interface.

By comparing Eqs. (61) and (64), one can see that in this regime the problem is local: the mass flux at coordinate x depends on the substrate and interfacial temperatures at the same point.

By combining Eq. (64) with Eqs. (37,61), one obtains the flux

$$J = \frac{\Delta T - \Delta p T_{sat}/(\mathcal{L}\rho_L)}{\mathcal{L}(R^i + h/k_L)} - \frac{T_{sat}}{2\mathcal{L}^4\rho_V^2} \frac{(\Delta T - \Delta p T_{sat}/(\mathcal{L}\rho_L))^2}{(R^i + h/k_L)^3}. \tag{65}$$

under an assumption that the vapor recoil term in Eq. (37) is small (which is true in most cases).

All the terms of the fourth order set of differential equations (49, 51) for the unknown functions $h(x)$ and $\Delta p(x)$ are now completely defined.

2.1 Fourth boundary condition for the case of pure vapor

To provide the temperature continuity, the interfacial temperature should be equal to that of the solid at the contact line. Eq. (37) thus results in

$$\Delta p(x \to 0) = \frac{\mathcal{L}\rho_L}{T_{sat}}(\Delta T - R^i J(x \to 0)\mathcal{L}) - \frac{J(x \to 0)^2 \rho_L}{2}\left(\frac{1}{\rho_V^2} - \frac{1}{\rho_L^2}\right). \tag{66}$$

Similarly to sec. 1.4, to obtain $J(x \to 0)$, Eq. (49) (now containing the Marangoni term) is integrated from 0 to x, where x is infinitesimally small. This results in

$$-\gamma \frac{\partial T^i}{\partial x} + \theta_{micro} x \frac{\partial \Delta p}{\partial x} = \frac{\mu}{l_s \theta_{micro}} \left[\theta_{micro} v_{CL} - \frac{J)}{\rho_L}\right]. \tag{67}$$

The T^i derivative can be obtained by developing Eq. (64) into the Taylor series around $h = 0$:

$$\frac{\partial T^i}{\partial x} = -\frac{\mathcal{L}\theta_{micro}}{k_L} J, \tag{68}$$

where Eq. (61) is accounted for. The substitution into Eq. (67) results in the expression

$$x\frac{\partial \Delta p}{\partial x} = \frac{\mu}{l_s \theta_{micro}} \left[v_{CL} - J \left(\frac{1}{\theta_{micro}\rho_L} + \frac{l_s \mathcal{L}\theta_{micro}}{\mu k_L}\gamma \right) \right]. \tag{69}$$

By injecting the value of J from Eq. (65) into Eq. (69) one obtains a differential equation for Δp. Its solution [25] is quite straightforward and for this reason is not detailed here. From it, one obtains explicitly that Δp saturates at $x \to 0$ so Eq. (59) indeed holds. Note that such a behavior is different from the CL dynamics [18] for nonvolatile liquids, where the pressure boundary condition cannot be written and the limit (59) is nonzero.

Finally, Eqs. (59, 69) result in

$$J(x \to 0) = v_{CL} \left(\frac{1}{\theta_{micro}\rho_L} + \frac{l_s \mathcal{L}\theta_{micro}}{\mu k_L}\gamma \right)^{-1}. \tag{70}$$

The pressure boundary condition is easily obtained by substitution of Eq. (70) into Eq. (66).

In the particular case of the immobile contact line, $J(x \to 0)$ and

$$\Delta p(x \to 0) = \frac{\mathcal{L}\rho_L \Delta T}{T_{sat}}. \tag{71}$$

This formula is similar to the complete wetting case [47]. In such a situation, J also vanishes at the left domain border (which corresponds to the flat film at $x \to -\infty$, cf. Fig. 4a). In this case, the boundary condition exactly coincides with the condition (71) written however for $x \to -\infty$. Note that for $R^i = 0$ and when the vapor recoil effect is neglected, Eq. (71) describes also the moving CL case, cf. Eq. (66).

The evaporation flux (70) is proportional to v_{CL}. When the contact line advances ($v_{CL} < 0$), the heat flux at the CL becomes negative. It means that $J(x)$ changes sign and condensation occurs in an extremely small vicinity of the CL.

As the fourth boundary condition, one can use either the pressure derivative (59) or directly the pressure value (66) with the substitution of the mass flux (70).

2.2 Asymptotic analysis for immobile contact line

The asymptotic analysis is helpful to provide some general idea of the behavior of the apparent contact angle because it results in analytical expressions. It is possible for some simple problem statements, by neglecting most physical effects.

2.2.1 Partial wetting and small superheating

One of the main goals of a microregion model is the apparent contact angle. It turns out to be possible to obtain an analytic result for its variation with ΔT when it is small enough. This result is possible to be obtained for the "minimal complexity" problem, while accounting only for the Kelvin effect, which is auto-sufficient to relax the contact line singularity mentioned in sec. 1.1. The set of equations to be solved is the following:

$$\sigma \frac{\partial^2 h}{\partial x^2} = \Delta p, \tag{72a}$$

$$\frac{\partial}{\partial x}\left(\frac{h^3}{3}\frac{\partial \Delta p}{\partial x}\right) = \mu \frac{k_L T_{sat}}{\mathcal{L}^2 \rho_L^2} \frac{\Delta p - \mathcal{L}\rho_L \Delta T / T_{sat}}{h} \tag{72b}$$

with the boundary conditions (55, 56, 71). The scales $\sigma/(\mathcal{L}\rho_L)$, $\mathcal{L}\rho_L$ and T_{sat} are used to make the lengths, the pressure jump and the superheating dimensionless, respectively. The dimensionless counterparts of Eqs. (72) read

$$\frac{\partial^2 \tilde{h}}{\partial \tilde{x}^2} = \Delta \tilde{p}, \quad \frac{\partial}{\partial \tilde{x}}\left(\frac{\tilde{h}^3}{3}\frac{\partial \Delta \tilde{p}}{\partial \tilde{x}}\right) = N \frac{\Delta \tilde{p} - \varepsilon}{\tilde{h}}, \tag{73a}$$

$$\Delta \tilde{p}(\tilde{x} \to \infty) = 0, \tag{73b}$$

$$\tilde{h}(\tilde{x} = 0) = 0, \quad \Delta \tilde{p}(\tilde{x} = 0) = \varepsilon, \tag{73c}$$

$$\partial \tilde{h}/\partial \tilde{x}|_{\tilde{x}=0} = \theta_{micro}, \tag{73d}$$

where $N = \mu k_L T_{sat}/\sigma^2$ and $\varepsilon = \Delta T / T_{sat}$.

We seek a solution by expanding the pressure jump $\Delta \tilde{p}$ and shape $\tilde{h}$ in a regular perturbation series in ε [25]:

$$\Delta \tilde{p} = \tilde{p}_0 + \varepsilon \tilde{p}_1 + O(\varepsilon^2), \quad \tilde{h} = \tilde{h}_0 + \varepsilon \tilde{h}_1 + O(\varepsilon^2). \tag{74}$$

One needs to substitute (74) into the set (73) and collect terms of the same order in ε. In the zeroth order one obtains $\tilde{p}_0 = 0$ and $\tilde{h}_0 = \theta_{micro}\tilde{x}$.

The equation for $\tilde{p}_1$

$$\tilde{h}_0 \frac{\partial}{\partial \tilde{x}}\left(\tilde{h}_0^3 \frac{\partial \tilde{p}_1}{\partial \tilde{x}}\right) = \alpha^2 (\tilde{p}_1 - 1), \tag{75a}$$

$$\tilde{p}_1(\tilde{x} = 0) = 1, \tag{75b}$$

$$\tilde{p}_1(\tilde{x} \to \infty) = 0, \tag{75c}$$

where $\alpha = \sqrt{3N}/\theta_{micro}^2$, does not contain $\tilde{h}_1$. One can easily obtain its solution (e.g. with the Wolfram MATHEMATICA software) in terms of the modified Bessel functions I_1, K_1 of the first order

$$\tilde{p}_1(\tilde{x}) = 1 + C_1 \frac{K_1(\alpha/\tilde{x})}{\tilde{x}} + C_2 \frac{I_1(\alpha/\tilde{x})}{\tilde{x}}. \tag{76}$$

where C_1, C_2 are integration constants. Since $I_1(\cdot)$ diverges at infinity, the boundary condition (75b) requires $C_2 = 0$. Since $K_1(z \to 0) \sim z^{-1}$, the second constant $C_1 = \alpha$ is determined from (75c); the solution for $\Delta\tilde{p}(\tilde{x})$ is thus

$$\Delta\tilde{p} = \varepsilon - \varepsilon\frac{\alpha}{\tilde{x}}K_1\left(\frac{\alpha}{\tilde{x}}\right) + O(\varepsilon^2). \tag{77}$$

The condition (75b) turns out to be satisfied automatically since $K_1(z \to \infty) \to 0$ exponentially. According to Eqs. (73a), the slope at infinity can be found by integrating $\Delta\tilde{p}$,

$$\theta_{app} = \theta_{micro} + \alpha\varepsilon\int_0^\infty \left[\frac{1}{z^2} - \frac{1}{z}K_1(z)\right]\mathrm{d}z = \theta_{micro} + \frac{\alpha\varepsilon\pi}{2}.$$

By returning to the dimensional variables, one obtains the final expression for the apparent contact angle in terms of the microscopic contact angle within the first order approximation:

$$\theta_{app} = \theta_{micro} + \frac{\pi\Delta T}{2\sigma\theta_{micro}^2}\sqrt{\frac{3\mu k_L}{T_{sat}}}. \tag{78}$$

One can see that θ_{app} varies linearly with the superheating. Note that the slope diverges for $\theta_{micro} \to 0$, i.e. the complete wetting, which is a well-known behavior [47]. The asymptote (78) is shown in Fig. 10c below.

A similar result can be obtained in the framework of another approach where the Kelvin effect is neglected but both the hydrodynamic slip (sec. 1.2.1) and interfacial thermal resistance (sec. 1.2.5) are accounted for [24]:

$$\theta_{app} = \theta_{micro} + \frac{3\mu\Delta T}{\rho_L\mathcal{L}\sigma\theta_{micro}^3 R^i}f\left(\frac{l_s}{R^i k_L}\right),$$

where $f(\cdot)$ is a function of the order one. Note that the simultaneous introduction of both these effects is necessary to relax the contact line singularity. It is even possible to extend this result for larger ΔT [3, 19]:

$$\theta_{app}^4 = \theta_{micro}^4 + \frac{12\mu\Delta T}{\rho_L\mathcal{L}\sigma R^i}\log\left(\frac{e\theta_{micro}l_s}{\theta_{app}R^i k_L}\right). \tag{79}$$

However, a practical implementation of this model is more complex than the approach based on the Kelvin effect.

2.2.2 Partial wetting and large superheating

We consider again the set (72) but use a different scaling of variables [28]. To find it, one introduces $\theta_{app}\ell_K$ as a reference value for h, where ℓ_K is a reference value for x. By balancing two Δp-containing terms in Eq. (72b) (the third term is not meaningful

as it can be easily eliminated by shifting of Δp by $\Delta p(x \to 0)$), one gets

$$\ell_K = \frac{\sqrt{3\mu k_L T_{sat}}}{\theta_{app}^2 \rho_L \mathcal{L}}. \tag{80}$$

We therefore make the solution dimensionless using

$$h = \theta_{app} \ell_K \tilde{h}(\tilde{x}) \ , \quad \tilde{x} = x/\ell_K,$$

The dimensionless governing equations have the same form as (73a-73c), where N is now replaced by 1, and the superheating parameter becomes

$$\varepsilon = \frac{\sqrt{3\mu k_L T_{sat}}}{\sigma \theta_{app}^3} \ \frac{\Delta T}{T_{sat}} \tag{81}$$

The boundary condition (73d) is replaced by

$$\partial \tilde{h}/\partial \tilde{x}|_{\tilde{x}=0} = \theta_{micro}/\theta_{app}. \tag{82}$$

Like in the previous section, one can proceed by expanding both $\Delta\tilde{p}$ and $\tilde{h}$ in a regular perturbation series in ε. The solution for $\Delta\tilde{p}$ is just like in the previous section:

One mentions that, with the present scaling, the boundary condition (73b) is equivalent to $\tilde{h}'(\tilde{x} \to \infty) = 1$. Therefore, by using this expression to define a background solution, the asymptotic expansions are

$$\Delta\tilde{p} = \varepsilon \tilde{p}_1 + O(\varepsilon^2), \quad \tilde{h} = \tilde{x} + \varepsilon \tilde{h}_1 + O(\varepsilon^2). \tag{83}$$

The solution is exactly like (77) but with $\alpha = 1$. It can be integrated from ∞ to 0,

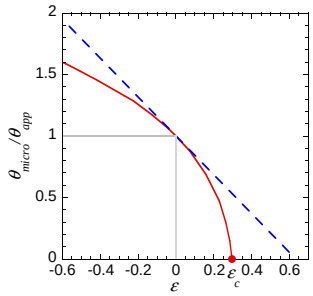

Fig. 7 Ratio of the microscopic and apparent contact angles as a function of the superheating parameter. Numerical solution: solid line; asymptotic expansion (84): dashed line.

which results in

$$\frac{\theta_{micro}}{\theta_{app}} = 1 - \frac{\pi}{2}\varepsilon + O(\varepsilon^2), \tag{84}$$

shown as a dashed line in Fig. 7.

The most important feature of the curve $\theta_{micro}/\theta_{app}(\varepsilon)$ is the existence of a terminal point $\varepsilon_c \simeq 0.297$; note that the linear approximation (84) overestimates ε_c by a factor $\simeq 2$. When ε approaches ε_c, $\theta_{app} \gg \theta_{micro}$, which means that the terminal point can be interpreted as corresponding to the large ΔT asymptotics. If one fixes $\varepsilon = \varepsilon_c$ in Eq. (81), the asymptotic expression for large ΔT follows:

$$\theta_{app} = \left(\frac{\sqrt{3\mu k_L T_{sat}}}{\varepsilon_c \sigma} \frac{\Delta T}{T_{sat}} \right)^{1/3} . \tag{85}$$

It is natural that at large ΔT, θ_{app} becomes independent of θ_{micro}, i.e. of its value at $\Delta T = 0$. This asymptote is shown in Fig. 10c below.

From Fig. 7, the terminal point corresponds to $\theta_{micro} = 0$, which means that Eq. (85) is the *exact* solution corresponding to this case. Since θ_{app} is an increasing function of θ_{micro} at a fixed ΔT, Eq. (85) provides the precise lower bound for θ_{app} for a given ΔT.

It should be stressed that the specific asymptotic expressions for θ_{app} may be invalid when other microscopic effects are accounted for. However the general tendency suggested by the asymptotic formulas remains valid. Among such general features one can list

- fast growth with ΔT for small ΔT and much weaker growth at large ΔT,
- strong dependence on θ_{micro} for small ΔT and a weaker dependence for large ΔT,
- increase of the difference $\theta_{app} - \theta_{micro}$ with μ and decrease with σ.

2.3 Parametric study of the apparent contact angle

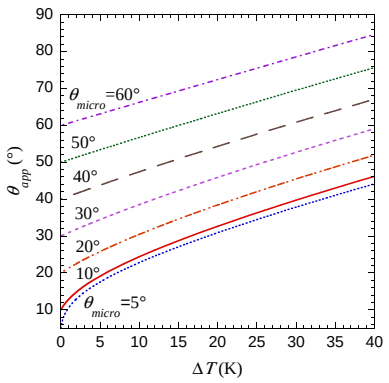

Fig. 8 Variation of the apparent contact angle with ΔT for different microscopic contact angle θ_{micro} for water at 1 atm and $l_s = 10$ nm.

In addition to what was mentioned above, in this section we discuss the impact of other parameters on the apparent contact angle for the case of the immobile CL (in which case the apparent and Voinov angles coincide, see sec. 2.4 below). In general all the fluid parameters impact the apparent contact angle. But some influence stronger than others. The following study has been conducted to show their impact and explain what it is.

The influence of two most important parameters, namely the solid superheating ΔT and the microscopic contact angle θ_{micro} is shown in Fig. 8. These curves have been calculated with the above model for the fluid parameters assumed constant. The situation shown in Fig. 8 is quite common: θ_{app} grows with both θ_{micro} and ΔT.

In the following, we discuss the impact of various microscopic-scale physical phenomena on the behavior of various parameters in the microregion, including the most important of them, the apparent contact angle. Unless mentioned specifically, the numerical calculations discussed here [23] are performed for water at 10 MPa, $\theta_Y = 15°$, $l_s = 10$ nm. We use the equations (72) as a reference and add various effects to study their impact.

2.3.1 Impact of surface forces for partial wetting

The surface forces can be introduced into the partial wetting theory as explained in sec. 1.2.3, with the regularized at $h \to 0$ disjoining pressure (20). Note that, as mentioned in sec. 1.2.3, the disjoining pressure leads to the difference between θ_{micro}, i. e. the slope at a scale smaller than that of the surface forces, and θ_Y, i.e. the static equilibrium contact angle at a larger (but still nanometer) scale.

The numerical calculations discussed here [26] use the following values related to the surface forces: $\theta_{micro} = 1°$, $h_m = 1$ nm and $A = 3.7 \cdot 10^{-20}$ J.

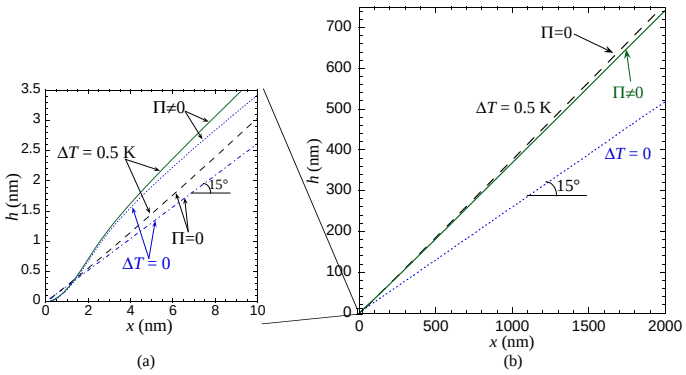

Fig. 9 Wedge shape computed for $\theta_Y = 15°$ with and without the impact of surface forces. (a) Close nanometric vicinity of the contact line. (b) Large scale view [23].

Examples of the computed shape of the liquid-vapor interface with and without accounting for the disjoining pressure effect are shown in Fig. 9. One can see that the macroscopic shapes in Fig. 9b for the cases $\Pi = 0$ and $\Pi \neq 0$ are very close. The curves corresponding to $\Pi = 0$ and $\Pi \neq 0$ are indistinguishable at this scale for $\Delta T = 0$. The impact of the surface forces is visible (Fig. 9a) only on a scale comparable to the characteristic scale (cf. sec. 2.2.2)

$$\ell_K^{micro} = \frac{\sqrt{3\mu k_L T_{sat}}}{\theta_{micro}^2 \rho_L \mathcal{L}}, \tag{86}$$

which is $\simeq 7.2$ nm here. The wedge shape follows the trend schematized in Fig. 4. One can check that the variation of the parameters A, h_m and θ_{micro} at a fixed θ_Y do not impact the apparent contact angle either [23]. For this reason, in the remaining part of this chapter we neglect the surface forces, so $\theta_{micro} = \theta_Y$ according to Eq. (19).

2.3.2 Impact of the slip length

When using the scaling based on ℓ_K^{micro} (86), the governing equation including the slip length can be reduced to the following form using an approach like in sec. 2.2.2:

$$(\tilde{h} + \mathcal{R}) \frac{\partial}{\partial \tilde{x}} \left[\left(\beta \tilde{h}^2 + \tilde{h}^3 \right) \frac{\partial^3 \tilde{h}}{\partial \tilde{x}^3} \right] = \frac{\partial^2 \tilde{h}}{\partial \tilde{x}^2} - \varepsilon^{micro},$$

where the slip parameter is

$$\beta = 3 l_s / (\theta_{micro} \ell_K^{micro}).$$

$$\varepsilon^{micro} = \frac{\sqrt{3\mu k_L T_{sat}}}{\sigma \theta_{micro}^3} \frac{\Delta T}{T_{sat}}$$

is the dimensionless superheating, and

$$\mathcal{R} = \frac{l_R}{\theta_{micro} \ell_K^{micro}}. \tag{87}$$

is the dimensionless interfacial resistance (cf. sec. 1.2.5). The scale $l_R = R^i k_L$ is an equivalent thickness of the liquid layer of the thermal resistance R^i. As an example, $l_R = 2$ nm for water at 10 MPa, with R^i given by Eq. (36). The constraint $\mathcal{R} = 0$ is artificially imposed here to show the impact of the slip length alone; the impact of R^i is considered in the next section. Consequently, ε_{micro} and β are the only parameters defining the behavior of the system.

One can argue that the scales considered in Fig. 10a are too small to be physically reasonable within a continuum medium approach. The resolving such small scales is however necessary to find a correct solution at a larger x.

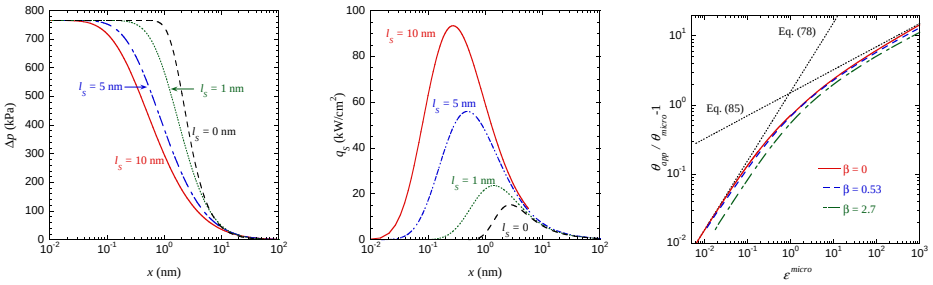

(a) Pressure jump spatial variation for water at 10 MPa, ΔT = 0.5 K, θ_{micro} = 15°.

(b) Heat flux spatial variation for water at 10 MPa, ΔT = 0.5 K, θ_{micro} = 15°.

(c) θ_{app} as a function of the dimensionless superheating ε^{micro} for different β. The asymptotic solutions (78, 85) are also shown.

Fig. 10 Pressure and heat flux spatial variations and the apparent contact angle as a function of superheating for different slip lengths; $\mathcal{R} = 0$ [23].

The hydrodynamic slip is well-known to remove the CL singularity for moving contact line (in the absence of the Kelvin effect). In case of its implementation for the evaporation with immobile CL [19, 24], similarly to the moving CL case, one obtains the logarithmically divergent $\Delta p(x \to 0)$. While such a divergence is integrable (it does not case the divergence of integral properties like viscous energy dissipation) this is still nonphysical as the pressure, being a measurable quantity, cannot be infinite. The Kelvin effect causes the finite pressure at CL, which is more coherent from the physical viewpoint. With l_s increase, Δp decays slower along the wedge (Fig. 10a) so in the limit $\beta \to \infty$ the dependence $\Delta p(x)$ approaches a straight line in the semi-logarithmic scale (indicating the logarithmic pressure divergence) and the pressure saturation at $x \to 0$ eventually disappears in the limit $\beta \to \infty$. For a fixed x, the pressure jump thus reduces with the l_s increase. Since θ_{app} is proportional to $\int_0^\infty \Delta p(x)dx$, it decreases with l_s (Fig. 10c).

The liquid-vapor interface heat flux variation along the liquid wedge (Fig. 10b) shows huge heat fluxes localized however in a tiny CL vicinity. The maximum of the local heat flux increases with the slip length. This is due to the fact that pressure jump (and thus the interface temperature) both saturate at a smaller scale, where the liquid thickness (and thus the conductive thermal resistance) are smaller so the flux is larger. However such flux increase is not strong enough to cause the pressure increase. In Fig. 10c the curves $\theta_{app}/\theta_{micro} - 1$ vs. ε^{micro} are compared for three values of β = 0, 0.53 and 2.7. The slopes of the curves for small and large ε_{micro} are close to those for the case $\beta = 0$ described by Eqs. (78, 85). It is evident that the apparent contact angle decreases with the slip length, however the impact of the slip length is weak for $\beta < 1$. This is an expected behavior as the crossover to the regime controlled by the slip rather than Kelvin effect is expected at $\beta \sim 1$, cf. Fig. 11c below.

2.3.3 Impact of the interface thermal resistance

The impact of the interface thermal resistance R^i (see section 1.2.5) is studied here. Fig. 11a shows the interfacial heat flux variation along the liquid wedge for four different l_R values. The length scale at which the flux maximum is attained, remains nearly unaffected by R^i. As expected, the interfacial resistance causes the heat flux reduction. Consequently, the pressure drop becomes smaller, which leads to a smaller apparent contact angle (see Figs. 11b, 11c).

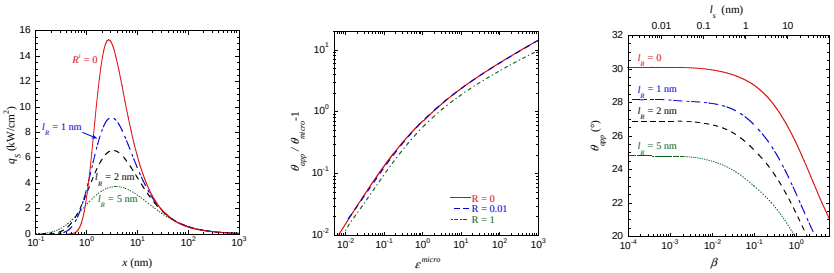

(a) Heat flux spatial variation for $l_s = 0$ and different l_R.

(b) θ_{app} as a function of superheating for $l_s = 0$ and different $\mathcal{R}$.

(c) θ_{app} as a function of the slip parameter for different R^i.

Fig. 11 Impact of the interfacial kinetic resistance on the microregion parameters for water at 10 MPa and $\Delta T = 0.5$ K [23].

In Fig. 11b the variation of the parameter $\theta_{app}/\theta_{micro} - 1$ with the dimensionless superheating ε^{micro} is shown for three values of $\mathcal{R} = 0, 0.01$ and 1 (which correspond to $l_R = 0$, 1 nm and 10 nm for water at 10 MPa and $\theta_{micro} = 5°$). It is evident that the apparent contact angle decreases with $\mathcal{R}$, however the variation is weak. Similarly to Fig. 10c, the curves for $\mathcal{R} \neq 0$ look shifted with respect to the curve $\mathcal{R} = 0$. The slopes for small and large ε_{micro} seem to be the same as for the case $R^i = 0$. As for simultaneous account of R^i and l_s, they both lead to the θ_{app} reduction (Fig. 11c). An especially fast θ_{app} decrease starts from $\beta = 1$.

2.4 Simultaneous contact line motion and evaporation

The contact line receding is quite common at evaporation; its impact on the apparent contact angle thus needs to be investigated. The moving contact line problem is more complex than its static counterpart. The difficulty comes from the flow caused by the contact line motion that is not limited to close contact line vicinity. This becomes evident if one considers a liquid wedge moving along a solid, or rather solid moving with respect to the liquid wedge (which is equivalent). Because of the viscous forces, the liquid is drugged by the moving solid not only near the contact line, but all along

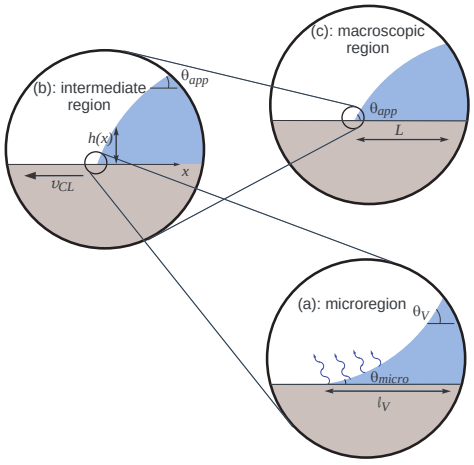

Fig. 12 Hierarchy of length scales in the moving CL problem with phase change.

the wedge. Thanks to the change of liquid thickness, the hydrodynamic stress caused by this motion appears to be large only in some vicinity of the contact line, which is however larger than the vicinity where the evaporation effects are important. One can show that, in general, three scales can be identified (Fig. 12) in the hierarchy. At the smallest scale, the mass exchange defines the interfacial curvature and the impact of the contact line motion is negligible. Therefore this region can be assimilated to the microregion considered for the immobile contact line (Fig. 12a). Its characteristic size will be called the Voinov length $\ell_V \sim 100$ nm for the reasons that will be evident later on. The macroscopic length scale L is governed by the capillarity and gravity forces, and possibly the macroscopic fluid motion around the drop or the bubble (Fig. 12c). Typically, $L \sim 1$ mm, but it depends on the problem. In between these two scales lies an intermediate region (Fig. 12b) where the impact of mass exchange is negligible and the interfacial profile is defined by the flow caused by the contact line motion; the relevant phenomena here are the surface tension and viscosity.

Eq. (49) can describe all the above scales (of course, within the limits of applicability of the lubrication approximation). If the gravity or other external forces are important, they should be included into the equation. There are two possible ways of solving such a problem. In principle, one can calculate it straightforwardly by numerics. However this is not easy as one needs to resolve both small and large scales, which requires application of heterogeneous adaptive grids that are often cause numerical instabilities for these nonlinear differential equations. Alternatively, thanks to the strong scale difference between small and large scales, one can apply a multi-scale approach. It consist in using a mathematical method called asymptotic matching two times. First, one couples the micro and intermediate regions and then intermediate and macro regions to obtain the full solution.

2.4.1 Matching of microscopic and intermediate regions

The impact of the CL motion will be considered with the "minimal complexity" set of equations, where among all the microscopic phenomena, only the Kelvin effect is accounted for [28]. This means that the fluid flow in the wedge is described by Eq. (52) in the reference, where CL is immobile; the $\partial h/\partial t$ term is replaced by two terms (54). As the macroregion is not considered, the transient term can be neglected and only the v_{CL}-containing term remains:

$$\frac{\partial}{\partial x}\left(\frac{h^3}{3}\frac{\partial \Delta p}{\partial x}\right) = \mu v_{CL}\frac{\partial h}{\partial x} + \mu\frac{k_L T_{sat}}{\mathcal{L}^2\rho_L^2}\frac{\Delta p - \mathcal{L}\rho_L \Delta T/T_{sat}}{h}, \tag{88}$$

where Δp is defined by Eq. (72a), with the boundary conditions (55, 56, 71). While comparing two terms in the r.h.s. of Eq. (88), one can see that, at large h, the mass exchange term is small so the contact line motion term defines the wedge curvature. Inversely, near the contact line, the contact line motion term is smaller. This kind of behavior is typical for the multi-scale problems.

The asymptotic matching consists in solving two separate problems. The first is in the "inner" region (microregion in the first problem), and the second, in the "outer" region (intermediate region in the first problem). As discussed above, in the inner region, the problem (72) should be solved (i.e. Eq. (88) with no v_{CL} term), while in the outer, the equation

$$\sigma\frac{\partial}{\partial x}\left(\frac{h^3}{3}\frac{\partial^3 h}{\partial x^3}\right) = \mu v_{CL}\frac{\partial h}{\partial x} \tag{89}$$

satisfying the boundary condition (56). This problem describes the moving contact line with no phase change [17]. According to the asymptotic matching technique, the boundary conditions at $x \to \infty$ in the inner region should match to $x \to 0$ in the outer. They should be found during the solution.

After integrating once, Eq. (89) reduces to

$$\sigma\frac{\partial^3 h}{\partial x^3} = \frac{3\mu v_{CL}}{h^2}. \tag{90}$$

Such a problem has an asymptotic (Cox-Voinov) solution first found by Voinov [57] far from the contact line:

$$\left(\frac{\partial h}{\partial x}\right)^3 = \theta_V^3 - 9Ca\log\frac{x}{\ell_V} \tag{91}$$

where $Ca = \mu v_{CL}/\sigma$ is the capillary number. For the receding case ($Ca > 0$), the situation is more complex; Eq. (91) is valid when the second term on the right hand side is sufficiently smaller than the first (below the dynamic wetting transition [13, 52]) because otherwise it cannot be matched to the macroscopic region.

It is evident now that the Voinov contact angle θ_V is the slope at $x \to \infty$ for the micoregion problem, i.e. at $Ca = 0$. In our case, the slope given by the micoregion problem saturates at $x \to \infty$, i.e. corresponds to the apparent contact angle discussed

above. From now on, it is called θ_V as the apparent contact angle is a result of not only the evaporation but also the contact line motion (Fig. 12c).

2.4.2 Matching between microscopic and intermediate regions

The scaling

$$\ell_K = \frac{\sqrt{3\mu k_L T_{sat}}}{\theta_V^2 \rho_L \mathcal{L}},$$
$$h = \theta_V \ell_K \tilde{h}(\tilde{x}) \ , \quad \tilde{x} = x/\ell_K,$$

is similar to that defined in Eq. (80) (with θ_V equivalent to θ_{app} of sec. 2.2.2). The dimensionless governing equation reads

$$(\tilde{h}''' \tilde{h}^3)' = \delta \, \tilde{h}' + \frac{\tilde{h}'' - \varepsilon}{\tilde{h}}, \tag{92}$$

where

$$\varepsilon = \frac{\sqrt{3\mu k_L T_{sat}}}{\sigma \theta_V^3} \, \frac{\Delta T}{T_{sat}}$$

and

$$\delta = \frac{3Ca}{\theta_V^3}.$$

To solve this problem, we use an expansion

$$\tilde{h} = \tilde{h}_0 + \delta \, \tilde{h}_\delta + O(\delta^2).$$

The zeroth order corresponds to the equations considered in sec. 2.2.2. The first order equation solved in the outer region results in the linearized version

$$\tilde{h}' = 1 - \delta \log(\tilde{x} \ell_K / \ell_V). \tag{93}$$

of Eq. (91). The full numerical solution is the solid line in Fig. 13a. The full solution is shown here together with the inner and outer solutions. The curves are shown in semi-logarithmic scale, in which the outer solution (93) is a straight line. This line can be obtained as a fit of the full solution for large $\tilde{x}$. According to Eq. (93), the abscissa of the outer solution for $\tilde{h}' = 1$ gives the Voinov length ℓ_V. Its dependence on ε is shown in Fig. 13b.

The multi-scale approach developed above for the case of the Kelvin effect can be generalized for any microregion description. As shown above (cf. Snoeijer and Andreotti [52] for a review) the hydrodynamic flow generated at the intermediate length scale (say, in between 100 nm and 10 μm from CL, Fig. 12b) is independent of the specific details of the microregion and the relative contribution of different microscale effects discussed in sec. 1. In fact they influence the intermediate re-

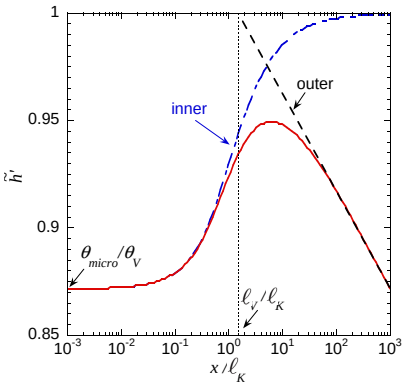

(a) Solution for $\varepsilon = 0.08$ and $\delta = -0.07$. The dash dotted line corresponds to the inner solution ($\delta = 0$). The dashed line corresponds to the outer solution (93).

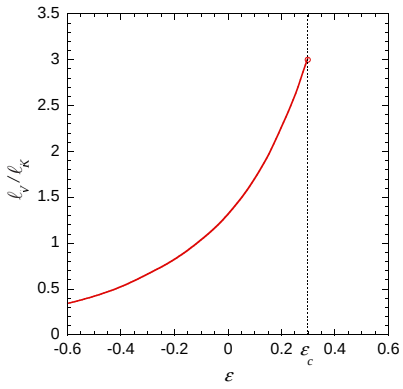

(b) The Voinov length ℓ_V as a function of the dimensionless superheating of the solid.

Fig. 13 Matching of the micro and intermediate regions [28].

gion through only two parameters, the Voinov length ℓ_V corresponding to the size of microregion and Voinov angle. The specific expression ℓ_V depends on the microregion model. For example, for the hydrodynamic slip model in isothermal case, $\ell_V = \ell_s = 3l_s/(e\ \theta_V)$ [13]. The complete wetting case is different because ℓ_V depends on the CL velocity: $\ell_V = 0.63(A/6\pi\sigma)^{1/2}/Ca^{2/3}$ [42].

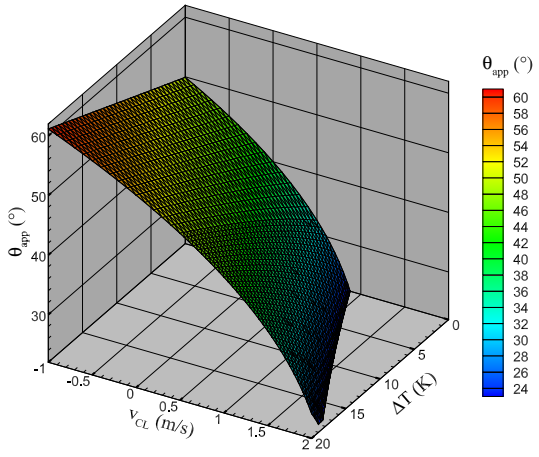

Fig. 14 θ_{app} as a function of the wall superheating ΔT and the CL velocity ($v_{CL} > 0$ at receding) calculated for water at atmospheric pressure; $x_{max} = 10\,\mu$m and $\theta_{micro} = 40°$.

Instead of using the above asymptotic matching approach, the set of equations (49, 51, 65) with the boundary conditions (55, 56, 66, 70) can be solved numerically for the system of interest. However, as Eq. (91) shows, the slope depends (although weakly) on the scale at which it is defined. As a macroscopic scale, one can use a fixed right boundary x_{max} of the integration domain so that the boundary condition (56) is imposed at $x = x_{max}$. An example of such a calculation is shown in Fig. 14. It can be checked [26] that it obeys the Cox-Voinov law.

2.4.3 Matching to macroscopic region: drop retraction

The Cox-Voinov law (91) is an extremely important result of matching of the microscopic and intermediate regions (cf. Fig. 12). However a definition of the apparent contact angle as a slope at a coordinate x is still vague as it depends (although weakly) on an unknown variable x. For practical applications, θ_{app} should thus be determined at a macroscopic scale. This means that the second matching procedure, between intermediate and macroscopic regions, should be applied. We discuss next an example of such a matching for the case of the drop geometry. It was first done by Pismen and Eggers [42] for the complete wetting case, with no mass exchange. We generalize it here for any microregion model, and show that it can be applied for the evaporation case (under an assumption).

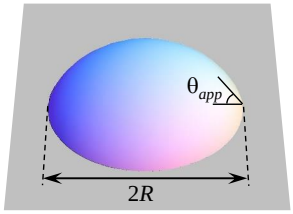

Fig. 15 Sessile drop on a flat substrate.

Consider a drop on a flat substrate (Fig. 15), small enough so the gravity does not impact its shape. Let it be out of equilibrium slowly spreading or retracting to gain an equilibrium shape, possibly due to the evaporation effect in the microregion. In the case of cylindrical symmetry, $h = h(r,t)$ (where $r = \sqrt{x^2 + y^2}$), the evaporation loss in the macroregion is neglected, and Eq. (53) reduces to

$$-3\frac{\mu}{\sigma}\frac{\partial h}{\partial t} = \frac{1}{r}\frac{\partial}{\partial r}\left\{rh^3\frac{\partial}{\partial r}\left[\frac{1}{r}\frac{\partial}{\partial r}\left(r\frac{\partial h}{\partial r}\right)\right]\right\}. \tag{94}$$

As previously, h is developed for small Ca,

$$h = h_0 + Cah_1 + O(Ca^2). \tag{95}$$

$Ca = \mu v_{CL}/\sigma$ is defined by using

$$v_{CL} = -\mathrm{d}R/\mathrm{d}t \tag{96}$$

in agreement with the adopted sign convention, where R is the radius of CL. As the drop dynamics is driven by the CL motion, it is evident that in the zeroth order, Eq. (94) reduces to

$$\frac{1}{r}\frac{\partial}{\partial r}\left(r\frac{\partial h_0}{\partial r}\right) = \text{const},$$

thus describing the spherical cap in a small-slope approximation:

$$h_0 = \frac{2V}{\pi R^2}\left(1 - \frac{r^2}{R^2}\right). \tag{97}$$

The drop volume

$$V = 2\pi \int_0^R hr\mathrm{d}r \tag{98}$$

is assumed to remain constant throughout CL motion, which means that the evaporation losses are small with respect to the drop mass. The apparent contact angle can now be clearly defined from this spherical cap shape as

$$\theta_{app} = -\left.\frac{\partial h_0}{\partial r}\right|_{r=R} = \frac{4V}{\pi R^3}. \tag{99}$$

One mentions that to the first order in Ca,

$$-\frac{\mu}{\sigma}\frac{\partial h}{\partial t} = Ca\frac{\partial h_0}{\partial R},$$

and Eq. (94) reduces to

$$3\theta_{app}\left(1 - 2\frac{r^2}{R^2}\right) = \frac{1}{r}\frac{\partial}{\partial r}\left\{rh_0^3\frac{\partial}{\partial r}\left[\frac{1}{r}\frac{\partial}{\partial r}\left(r\frac{\partial h_1}{\partial r}\right)\right]\right\}. \tag{100}$$

Instead of using the method of Pismen and Eggers [42], it is much simpler to integrate it directly by applying the boundary conditions at the contact line, the symmetry conditions at $r = 0$ and the mass conservation that follows from Eq. (98):

$$\begin{aligned} &h_1(r = R) = 0,\\ &\partial h_1/\partial r|_{r=0} = 0,\\ &\partial^3 h_1/\partial r^3|_{r=0} = 0,\\ &\int_0^R h_1 r\mathrm{d}r = 0. \end{aligned}$$

The result for the interface slope is

$$\frac{\partial h_1}{\partial r} = -\frac{3R}{r\theta_{app}^2}\left[2\frac{r^2}{R^2} + \log\left(1 - \frac{r^2}{R^2}\right)\right]. \tag{101}$$

For matching of this solution to the intermediate region, one needs to find its asymptotics at $x \simeq R - r \to 0$:

$$\left(\frac{\partial h}{\partial x}\right)^3 = \theta_{app}^3 - 9Ca\log\left(\frac{2e^2 x}{R}\right). \tag{102}$$

By equalizing this expression to Eq. (91) (which is the $x \to \infty$ asymptotics coming from the intermediate region), one obtains the final expression

$$\theta_{app}^3 = \theta_V^3 - 9Ca\log\left(\frac{L}{\ell_V}\right), \tag{103}$$

for the apparent contact angle, where the macroscopic scale $L = R/(2e^2)$ is now uniquely defined. Eq. (103) represents the final result of the multi-scale approach for the drop geometry; θ_{app} is now uniquely defined as a function of the system parameters.

Note that Eq. (103) can be used to describe the drop dynamics. The most well-known example is the drop spreading in the complete wetting case with no mass exchange, where $\theta_V = \theta_{micro} = 0$. By using the definitions (96, 99) one obtains from Eq. (103) the scaling

$$\frac{\mathrm{d}R}{\mathrm{d}t} \sim R^{-9},$$

that results in the Tanner law [17] $R \sim t^{1/10}$.

Eq. (103) clearly shows how the microregion impacts the macroscopic behavior. Two parameters come from the microregion, the Voinov angle θ_V and length ℓ_V. When $\Delta T = 0$ (no mass exchange), they are constant; $\theta_V = \theta_{micro}$. When $\Delta T \neq 0$, both these parameters depend on ΔT. The dependence $\theta_V(\Delta T)$ is the most important, cf. sec. 2.3. An example for the dependence of $\ell_V(\Delta T)$ provided by the Kelvin effect is shown in Fig. 13b.

2.4.4 Dewetting

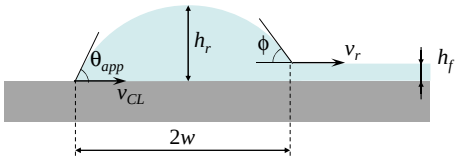

Fig. 16 2D Dewetting ridge.

In this section we briefly consider the dewetting phenomenon. Imagine a classical (isothermal) case of a liquid film with a straight contact line that forms on a flat surface e.g. during a receding of a liquid plug from a capillary slot. If the equilibrium contact angle is large, the CL moves thus leading to the reduction of the film interface energy. However the liquid cannot flow into the film because of the high viscous friction. The receding liquid forms thus a ridge (called also rim) at the film edge (Fig. 16). As the evaporation impacts the apparent contact angle, it is expected to impact the macroscopic ridge dynamics discussed next.

Brochard-Wyart et al. [7] have been first to develop a dewetting theory. Originally it was based on the phenomenological approach to the contact line motion [17]. For uniformity, it is presented here by using the above hydrodynamic theory that results in

$$\theta_{app}^3 = \theta_V^3 - \frac{v_{CL}}{v^*}, \tag{104}$$

where v^* is a constant (logarithmic) term. The theory is developed in the approximation of the small $\theta_{app} \ll 1$, so the slope ϕ of the rear edge of the ridge (Fig. 16) is equally small. It obeys a law similar to (104) but accounting for the fact that the equilibrium ϕ value is zero:

$$\phi^3 = \frac{v_r}{v^*}, \tag{105}$$

where v_r is the velocity of the rear ridge edge. As mentioned above, all the liquid from the film of the thickness h_f is gathered in the ridge so its area A (in the plane of Fig. 16) growth obeys the law $\dot{A} = v_r h_f$. Consider the late stages of the ridge growth, where its height $h_r \gg h_f$. The area is defined as $A \sim h_r w$, where w is the ridge half-width, so $\dot{A} \sim h_r \dot{w}$ for small θ_{app}. This means that

$$\frac{\dot{w}}{v_r} \sim \frac{h_f}{h_r} \ll 1,$$

which justifies that $v_{CL} = v_r - 2\dot{w} \simeq v_r$. Since $h_f \ll h_r$, $\theta_{app} \simeq \phi$. With two latter equalities, Eqs. (104, 105) reduce to $\theta_{app}^3 \simeq \theta_V^3/2$ and

$$v_{CL} \simeq \theta_V^3 \frac{v^*}{2}. \tag{106}$$

Eq. (106) is the central result of this phenomenological approach, which shows the $v_{CL} \propto \theta_V^3$ proportionality but is not able to predict the prefactor.

To obtain the prefactor, one needs a more sophisticated multi-scale theoretical approach [53] based on the asymptotic matching technique similar to that described for the drop case (sec. 2.4.3). An additional complication of the dewetting ridge geometry is its dissymmetry: one needs to match the ridge with the film of a finite (typically $\sim 50\,\mu$m) thickness. The matching is possible to do asymptotically under the above assumption $h_f \ll h_r$. The asymptotic model of Snoeijer and Eggers has been initially developed for the microregion model based on the hydrodynamic slip. Its main result can easily be generalized to a general microregion description as

$$Ca = \frac{\theta_V^3}{9}\left[\log\left(aCa^{1/3}\frac{w^2}{l_V h_f}\right)\right]^{-1}, \qquad (107)$$

where $a \approx 0.15$ is a matching constant. Eq. (107) defines the CL velocity. One can see its θ_V^3 behavior (106) predicted by the phenomenological theory. The apparent contact angle obeys Eq. (103), where the expression $L = w/e$ holds for the ridge case.

2.5 Comparison with experimental data

Some typical dependencies of θ_V on the wall superheating are shown in Fig. 17. Note that a strong change of the apparent contact angle for a reasonable superheating

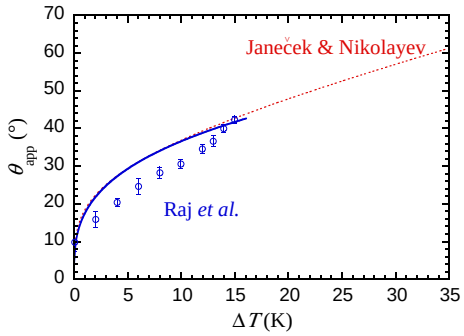

Fig. 17 The calculated dependency of θ_V on the wall superheating ΔT [27] calculated for the static contact angle for FC-72 at 0.04 MPa and $\theta_{micr} = 8°$ (dotted line) compared to the theoretical results for complete wetting Raj et al. [47], black solid line. Their experimental data (where $\theta = 8°$) are shown with circles.

of several tens of Kelvin characteristic to the boiling conditions. The agreement with the experimental data of Raj et al. [47] is reasonably good. The discrepancy between the experimental and theoretical data can probably be attributed to the neglect of the CL velocity (i.e. of the second term in Eq. (103)). The CL was moving in the experiment; the motion was not quantified by the authors and thus cannot be properly modeled.

The simultaneous phase change and CL motion was experimentally observed by Fourgeaud et al. [15] in a closed transparent sapphire capillary slot (Hele-Shaw cell) filled with pure ethanol. The sapphire substrate was heated by the electric current passed through a transparent indium-tin oxide film deposited on the back sapphire surface. A 60 μm thick ethanol film was laid down by a receding liquid. While the ethanol wets completely the sapphire at equilibrium, the dewetting phenomenon was observed at evaporation (Fig. 18a). The ridge shape was well-approximated by a

circular arc (except at late times where gravity played a role), from which θ_{app} and w were obtained.

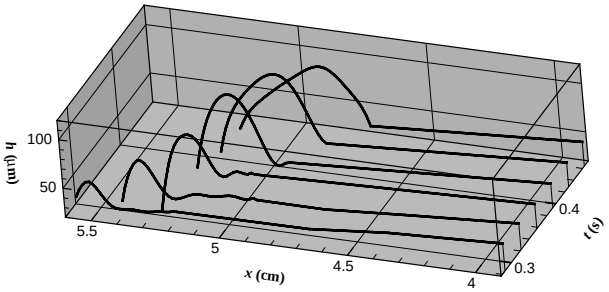

(a) The dewetting ridge dynamics caused by evaporation. The ridge shape is obtained with the optical methods.

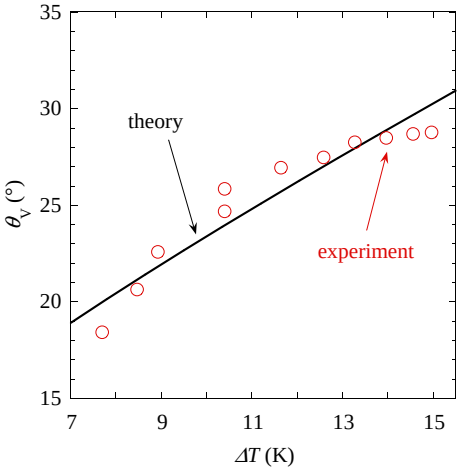

(b) The Voinov angle θ_V recalculated from experimental θ_{app} data versus wall superheating ΔT and the theoretical model.

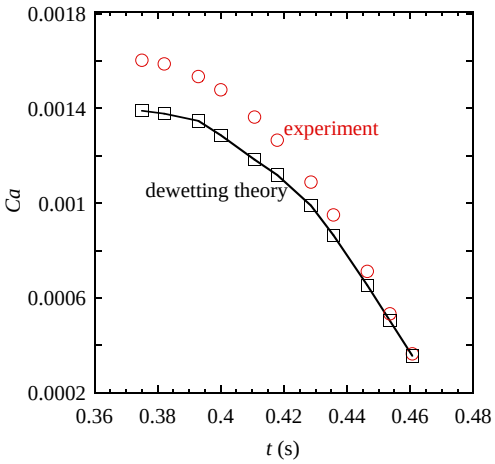

(c) Experimental data for the dimensionless CL velocity compared to the theoretical values given by Eq. (107).

Fig. 18 Evaporation-caused dewetting phenomenon. The dewetting theory results compared to experimental data on the ethanol film on sapphire [15].

The θ_V values (Fig. 18b) were calculated via Eq. (103) with $L = w/e$. According to estimations, $\ell_s \gg \ell_K$ for the ethanol, where the slip length $l_s = 20$ nm was used. For this reason, the hydrodynamic slip prevails over the Kelvin effect in the microregion and $\ell_V = \ell_s$ was assumed. The line in Fig. 18b is a theoretical curve similar to those of Fig. 8 calculated for the same parameters (including the same l_s). The agreement is very good, which shows the validity of the above theory. Fig. 18b shows that the θ_V values can be high in spite of nearly zero equilibrium contact angle. Such high θ_V values are at the origin of the solid wall dewetting.

Once a liquid film is deposited by the moving liquid meniscus, its CL is expected to recede because of two phenomena. First, according to the theory discussed above, the contact angle grows, and the substrate dewetting occurs. Second, the liquid in the CL vicinity vaporizes; there is no flow in the film so its length decreases; in other words, CL recedes because of the evaporative mass loss. Let us consider now the relative contribution of evaporative mass loss at the CL. Fig. 18c presents the experimental CL receding velocity together with the result of Eq. (107), which describes only the first (dewetting) contribution. One can see that in this particular experiment CL recedes mainly because of the contact angle growth via dewetting; the evaporative mass loss is responsible only for 14% of the CL velocity.

3 Diffusion-controlled evaporation

It has been shown experimentally [56] that the increase of apparent contact angle with evaporation rate exists in the case of isothermal drying in the atmosphere of a neutral gas. On can compare this case to the regime of evaporation to the pure vapor atmosphere induced by heating considered above. The theoretical description of drying is more complex as the mass exchange is controlled by the phenomena in the gas domain, which is generally much larger than the liquid domain that controls the pure vapor case so natural or forced convection is often important. Another reason of the increased complexity is the non-locality of evaporation flux: the evaporation rate at one point of the interface depends not only on the local vapor density, but on its distribution over the whole liquid-vapor interface. As the mass exchange rates are generally much smaller at drying, it is expected to be much weaker than in the pure vapor case. For this reason we consider this regime more briefly than the pure vapor case.

There are many theoretical approaches to the drying description. Early approaches neglect the impact of evaporation on the interface shape (and thus on the impact on contact angle). One of the first important steps was achieved by Deegan et al. [10] who have obtained the stationary diffusion problem solution in the half-space above a spherical-cap-shaped sessile liquid droplet posed on a solid substrate with a fixed contact angle. The success of this solution is due to the integrability of the resulting local evaporation flux so that the total evaporation rate can be calculated and compared to the experiment. The integrability of the background solution for the mass flux (i.e. a weaker divergence) is another reason of weaker effect of evaporation on the apparent contact angle in this regime comparing to the regime discussed in sec. 2.

In earlier theoretical approaches [5, 20, 41, 46], the evaporation flux distribution along the interface was imposed independently of the interface shape. The full coupling of the problems in the vapor and liquid phases through the Kelvin effect is studied in more recent works [11, 12, 14, 29, 36]. The Kelvin effect is important as it makes the evaporation flux to be finite at the contact line, cf. Eq. (58). It also causes the impact of evaporation on the apparent contact angle.

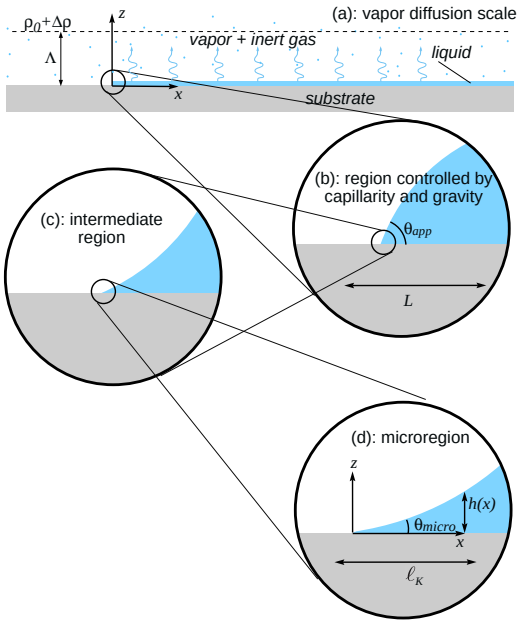

Fig. 19 Hierarchy of scales considered in the article and geometries for the vapor diffusion (a) and hydrodynamic (b-d) problems. Note that the radius of curvature in (b) is assumed to be much larger than the diffusive boundary layer width Λ shown in (a).

3.1 Problem statement

Consider a diffusion boundary layer of thickness Λ above the thin liquid wedge-like film. The value of Λ depends on the gas dynamics in the remaining part of the space (typically, natural or forced convection). The film is placed on a flat and homogeneous substrate in a situation of partial wetting. Its contact line is pinned; the problem of contact line motion under saturation conditions has been solved by Janeček et al. [29]. The atmosphere of a non-condensable inert gas surrounds the substrate and the condensation or evaporation mass exchange with it is controlled by the vapor transfer in the gas. The gas supersaturation with vapor causes condensation onto the film, and under-saturation causes its evaporation. The fluid is assumed to be isothermal, which may be justified when the substrate has a good thermal conductivity and is maintained at room temperature. For this reason, the temperature T is equivalent to T_{sat} used above.

First, some assumptions about the characteristic scale hierarchy need to be made. One can identify a macroscopic length scale L of the liquid phase. It is related to the macroscopic-level interface curvature, e.g. the interface curvature radius. Another macroscopic length scale concerns the gas phase description. It is the diffusion

boundary layer thickness Λ. It is millimetric (for natural convection) or smaller, for forced convection. For simplicity, we consider the diffusion boundary layer of homogeneous thickness (band-like). The idea is to find a stationary solution for the vapor diffusion that can be representative of real microscopic situation. For this we assume that

$$L \gg \Lambda \gg h \tag{108}$$

where h is the wedge thickness, see Fig. 19a,b. It is evident that the inequality (108) is violated far enough from the wedge apex (contact line) for any wedge slope. However, if the slope is small, the region of validity of such a geometry is large. As for the pure vapor case, the hydrodynamic singularity related to the evaporation flow is solved at the microscopic scale that we call ℓ_K which is typically nanometric (Fig. 19d). An intermediate region (Fig. 19c) is needed to match micro and macro regions. We will see later that, generally, in this case two intermediate regions need to be introduced.

The equation governing the liquid flow in the wedge is the stationary version of Eq. (52):

$$\frac{\partial}{\partial x}\left(\frac{h^3}{3}\frac{\partial \Delta p}{\partial x}\right) = -\mu\frac{J}{\rho_L}, \text{ where } \Delta p = \sigma K = \sigma\frac{\partial^2 h}{\partial x^2}. \tag{109}$$

The interfacial mass flux J is controlled by the vapor diffusion,

$$J = -D\left.\frac{\partial \rho_V}{\partial z}\right|_{z=0}, \tag{110}$$

where $\rho_V = \rho_V(x,z)$ now varies in space and D is the coefficient of the vapor diffusion in the ambient gas. The vapor diffusion equation reads

$$\frac{\partial^2 \rho_V}{\partial x^2} + \frac{\partial^2 \rho_V}{\partial z^2} = 0. \tag{111}$$

The boundary conditions for the liquid phase are as discussed in sec. 1.4: $h(x \to 0) = 0$ and $\partial h/\partial x|_{x\to 0} = \theta_{micro}$ at the CL, the vanishing curvature for from CL, $K(x \to \infty) = 0$, and the regularity of all hydrodynamic quantities at the CL equivalent to $J(x \to 0) = 0$.

Within the small wedge slope approximation, the liquid-gas interface seen from the large scale of the gas atmosphere is assumed to coincide with the line $z = 0, x \geq 0$, as shown in Fig. 19a. This assumption is valid for a liquid height much lower than the boundary layer thickness, i.e. for $x \ll \Lambda/\theta_{micro}$. As θ_{micro} is a small angle, the model is valid over a distance to the contact line much larger than Λ. The boundary conditions for the diffusion equation are defined at the upper and lower boundaries of the diffusion layer. At the upper boundary $z = \Lambda$,

$$\rho_V(x, z = \Lambda) = \rho_0 + \Delta\rho, \tag{112}$$

where ρ_0 is the vapor density at thermodynamic equilibrium for a flat liquid-gas interface, $\Delta\rho$ is the deviation from the equilibrium vapor density; $\Delta\rho < 0$ corresponds

to evaporation. The vapor cannot penetrate into the solid boundary ($z = 0$ and $x < 0$),

$$\frac{\partial \rho_V}{\partial z} = 0. \tag{113}$$

The vapor density at the liquid-gas interface can deviate from ρ_0 because of two reasons: (i) the interfacial pressure jump (Kelvin effect) and, (ii) because of the interfacial kinetic resistance R^i_{diff} defined by Eq. (34), so Eqs. (12, 32) can be combined so the boundary condition

$$\rho_V(x, z = 0) = \rho_0 - \Delta p \frac{M\rho_0}{\rho_L R_g T} - J R^i_{diff}, \tag{114}$$

is valid for $x \geq 0$. In the following sections we focus on the diffusion controlled regime; the impact of the kinetic interfacial resistance is analyzed by Doumenc et al. [12].

3.2 Kelvin effect and dimensionless formulation

The microregion size (Fig. 19) for the case of the singularity relaxation with the Kelvin effect can be easily obtained with a scaling analysis [29], that results in

$$\ell_K = \frac{1}{\rho_L}\sqrt{\frac{3\mu M \rho_0 D}{\theta^3_{micro} R_g T}}. \tag{115}$$

For the analysis below, the dimensionless abscissa is $\tilde{x} = x/\ell_K$. The liquid height is scaled as $\tilde{h} = h/(\theta_{micro}\ell_K)$, and the dimensionless flux is $\tilde{J} = 3\mu J/(\theta^4_{micro}\sigma\rho_L)$. The dimensionless lubrication equation reads

$$\frac{\partial}{\partial \tilde{x}}\left(\tilde{h}^3 \frac{\partial^3 \tilde{h}}{\partial \tilde{x}^3}\right) = -\tilde{J}. \tag{116}$$

Density deviation is reduced as $\tilde{\rho} = (\rho_V - \rho_0)/C$, with

$$C = \frac{\rho_L \sigma \theta^4_{micro} \ell_K}{3\mu D}. \tag{117}$$

The z and Λ variables are reduced with ℓ_K and the dimensionless boundary conditions for the diffusion problem for $\tilde{z} = 0,\ \tilde{x} \geq 0$ are

$$\frac{\partial \tilde{\rho}}{\partial \tilde{z}} = -\tilde{J}, \tag{118}$$

$$\tilde{\rho} = -\tilde{h}''. \tag{119}$$

The trivial boundary condition (113) is valid for $\tilde{z} = 0,\ \tilde{x} < 0$.

3.3 Weak evaporation approximation

The deviation from equilibrium $\varepsilon = \Delta\rho/C$ is assumed to be small; the variables are expanded in a regular perturbation series. At the zero order corresponding to the straight wedge in thermodynamic equilibrium, $\tilde{h}_0 = \tilde{x}$, $\tilde{J}_0 = 0$ and $\tilde{\rho}_0 = 0$;

$$\tilde{h} = \tilde{x} + \varepsilon\tilde{h}_1 + O(\varepsilon^2), \quad \tilde{J} = \varepsilon\tilde{J}_1 + O(\varepsilon^2), \quad \tilde{\rho} = \varepsilon\tilde{\rho}_1 + O(\varepsilon^2).$$

Note that ε is negative during evaporation and positive during condensation so $\tilde{J}_1$ and $\tilde{h}_1$ are always negative.

The first order problem is described by the fluid flow equation

$$\frac{\partial}{\partial\tilde{x}}\left(\tilde{x}^3\frac{\partial^3\tilde{h}_1}{\partial\tilde{x}^3}\right) = -\tilde{J}_1, \tag{120}$$

with the boundary conditions $\tilde{J}_1 = \tilde{h}_1 = \tilde{h}_1' = 0$ at $\tilde{x} = 0$ and $\tilde{h}_1'' = 0$ at $\tilde{x} \to \infty$. The diffusion part of the first order problem remains as above.

There is no analytical solution and the problem should be solved numerically. A direct numerical solution of the problem would be complicated as a nonlinear 1D fluid flow equation needs to be coupled to the 2D vapor diffusion problem in a stripe. For this reason, it is more convenient to solve the 2D problem analytically by using the boundary integral method. It consists in reducing the 2D differential equation (111) to the integral over the domain boundary by using the Green function [12]. By redefining the density variable as $\tilde{\rho}_1 - 1$, all the boundary conditions except those at $\tilde{z} = 0, \tilde{x} \geq 0$ become trivial; only the integral over this portion involves the boundary condition (118). The interfacial density $\tilde{\rho}_1(\tilde{x}, \tilde{z} = 0)$ over it can be expressed as a function of the mass flux as

$$\tilde{\rho}_1(\tilde{x}, \tilde{z} = 0) = 1 - \int_0^\infty G_0(\tilde{x} - \tilde{x}')\tilde{J}_1(\tilde{x}')\mathrm{d}\tilde{x}', \tag{121}$$

where

$$G_0(\tilde{x}) = \frac{1}{\pi}\log\left|\frac{\exp\left(\frac{\pi\tilde{x}}{2\tilde{\Lambda}}\right) - 1}{\exp\left(\frac{\pi\tilde{x}}{2\tilde{\Lambda}}\right) + 1}\right|$$

is the Green function.

By combining Eqs. (119-121), one gets a governing integral equation

$$\tilde{x}^3\int_0^\infty \frac{\partial G_0(\tilde{x} - \tilde{x}')}{\partial\tilde{x}}\tilde{J}_1(\tilde{x}')\partial\tilde{x}' = -\int_0^{\tilde{x}} \tilde{J}_1(\tilde{x}')\partial\tilde{x}' \tag{122}$$

that can be solved numerically [12]. Once $\tilde{J}_1$ is known, the slope can be computed with Eq. (120) integrated once.

3.4 Impact of the thickness of diffusion boundary layer

One of the most important parameters that impacts the evaporation rate and thus the apparent contact angle is the thickness Λ of the diffusion boundary layer; its impact is studied here.

Because of the presence of the length scale $\Lambda \gg \ell_K$, one identifies two intermediate regimes of different asymptotic behavior. The first intermediate region ranges from ℓ_K to Λ, while the second goes from Λ to L. As we do not discuss here the coupling to the macroregion, L is considered to be infinitely large.

Within both intermediate regions, the Kelvin effect can be neglected, which means that ρ_V at the interface is constant and equal to the saturation density ρ_0; $\tilde{\rho} = 0$. This is a "Deegan et al.-like" diffusion problem in the 2D boundary layer geometry admits an analytical solution [12]:

$$\tilde{J}_1(\tilde{x}) = -\frac{1}{\tilde{\Lambda}\sqrt{2}}\sqrt{1 + \coth\left(\frac{\pi\tilde{x}}{2\tilde{\Lambda}}\right)}. \tag{123}$$

Unfortunately, the fluid flow part of the problem, Eq. (120), cannot be solved analytically. For this reason the asymptotic solutions are considered. The asymptotic expressions for the flux are different for two intermediate regions. The limit $\tilde{x} \ll \tilde{\Lambda}$

$$\tilde{J}_1(\tilde{x}) \simeq -\frac{1}{\sqrt{\pi\tilde{\Lambda}\tilde{x}}}. \tag{124}$$

describes the first intermediate region, while the limit $\tilde{x} \gg \tilde{\Lambda}$

$$\tilde{J}_1(\tilde{x}) \simeq -\frac{1}{\tilde{\Lambda}}, \tag{125}$$

describes the second intermediate region. The scaling (124) was obtained by Deegan et al. [10] for the thin 3D axisymmetric drop and infinite boundary layer. However the present solution is different because the geometry is 2D, so the asymptotic solutions are always Λ-dependent (the solution for the stationary diffusion problem in 2D does not exist in the infinite domain). Instead of Λ, the solution of Deegan et al. is controlled by the drop diameter. The flux diverges at the contact line, as expected: it cannot describe the microregion dominated by the Kelvin effect.

One can get the curvature and the slope after successive integrations of Eq. (120) with the above asymptotic expressions for $\tilde{J}_1$ and by applying the boundary conditions to determine some of the integration constants [12].

Consider the first intermediate region $1 \ll \tilde{x} \ll \tilde{\Lambda}$. The asymptotic solution for the curvature is

$$\frac{\partial^2\tilde{h}_1}{\partial\tilde{x}^2} \simeq -\frac{4}{3}\frac{1}{\sqrt{\pi\tilde{\Lambda}\tilde{x}^3}}. \tag{126}$$

while the slope is

$$\frac{\partial \tilde{h}_1}{\partial \tilde{x}} \simeq \frac{8}{3}\frac{1}{\sqrt{\pi\tilde{\Lambda}}}\left(\frac{1}{\sqrt{\tilde{x}}} - \frac{1}{\sqrt{C_1}}\right), \tag{127}$$

where C_1 corresponds to the dimensionless size of the microregion, so $C_1 \sim 1$ is expected. For the second intermediate region $\tilde{\Lambda} \ll \tilde{x} \ll L$, by integrating Eq. (125), one gets

$$\frac{\partial^2 \tilde{h}_1}{\partial \tilde{x}^2} \simeq -\frac{1}{\tilde{\Lambda}\tilde{x}} \tag{128}$$

for the curvature and

$$\frac{\partial \tilde{h}_1}{\partial \tilde{x}} \simeq -\frac{1}{\tilde{\Lambda}}\left[\log\left(\frac{\tilde{x}}{\tilde{\Lambda}}\right) + C_2\right], \tag{129}$$

for the slope, with an integration constant C_2. At $\tilde{\Lambda} \gg C_1$, the slopes (127) and (129) should match at $\tilde{x} \sim \tilde{\Lambda}$. This results in

$$C_2 = C_3\sqrt{\tilde{\Lambda}/C_1} \tag{130}$$

with a constant $C_3 \sim 8/(3\sqrt{\pi}) \simeq 1.5$. Its exact value and those of the other constants can be determined by matching to the microregion model.

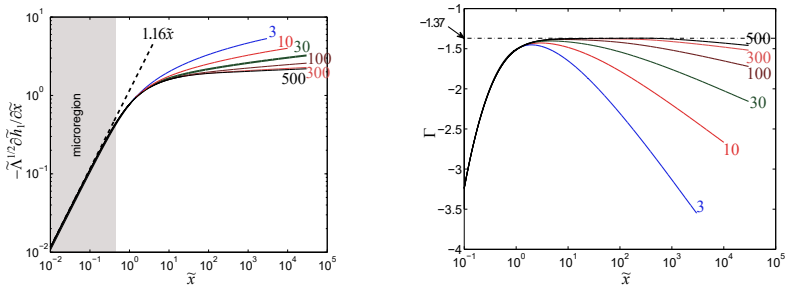

(a) The microregion slope behavior. The dashed line is the microregion asymptote.

(b) Solid lines are $\Gamma(\tilde{x})$ curves; dash-dotted line is the first intermediate region asymptote.

Fig. 20 Matching of microregion and first intermediate region [12] for different $\tilde{\Lambda}$.

The microregion asymptotic solution cannot be obtained analytically. Instead, the constants C_1 and C_2 that enter Eqs. (127, 129) are determined by solving numerically Eq. (122) valid in microscopic and both intermediate regions.

The numerics shows that in the microregion, $\partial\tilde{h}_1/\partial\tilde{x} \sim -\tilde{x}/\sqrt{\tilde{\Lambda}}$ (Fig. 20a). The $\tilde{\Lambda}^{-1/2}$ scaling is important to match the asymptotics (127) in the first intermediate region. The departure from the linear behavior corresponds to the end of microregion.

The first intermediate region is described by Eq. (127) that involves a characteristic length C_1. It can be obtained numerically by plotting (Fig. 20b) the quantity

$$\Gamma = 3/8(\pi\tilde{\Lambda})^{1/2}\frac{\partial\tilde{h}_1}{\partial\tilde{x}} - \tilde{x}^{-1/2}$$

that is expected to be constant ($\Gamma = -C_1^{-1/2}$) in the first intermediate region, cf. Eq. (127). Fig. 20b shows the $\tilde{x}$-independent region only for $\tilde{\Lambda} \gg 1$, which is exactly the criterion of existence of the first intermediate region. From the numerical value $\Gamma \simeq -1.37$, one gets $C_1 \simeq 0.53$ so the precise microregion size is $0.53\ell_K$.

To analyze the large scale behavior (in the second intermediate region) one needs to renormalize the slope data of Fig. 20. It is done in Fig. 21a. Note that the microregion behavior cannot be seen on these curves (the scale is too large).

A logarithmic variation of $\partial\tilde{h}_1/\partial\tilde{x}$ is observed for $x > \Lambda$, as predicted by Eq. (129). The integration constant $C_2 = -\tilde{\Lambda}\frac{\partial\tilde{h}_1}{\partial\tilde{x}}(\tilde{x} = \tilde{\Lambda})$ is obtained by fitting Eq. (129) to the numerical results (see dashed lines in Fig. 21a) and taking the intersection of each fit with the dash-dotted line $\tilde{x} = \tilde{\Lambda}$. The parameter C_2 is given in Fig. 21b as a function of $\tilde{\Lambda}$. For $\tilde{\Lambda} \gg 1$, the law (130) indeed holds, $C_2 = \chi\sqrt{\tilde{\Lambda}}$, where $\chi = C_3/\sqrt{C_1} \simeq 2$ is a constant. By using $C_1 \simeq 0.53$ obtained above, one gets $C_3 \simeq 1.46$.

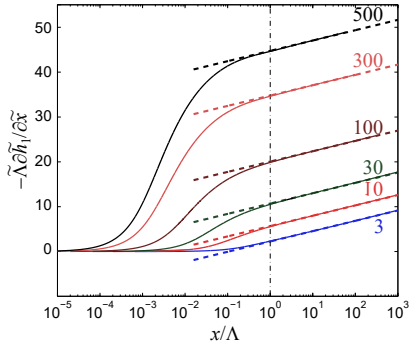

(a) Renormalized interface slope for different values of $\tilde{\Lambda}$; solid lines: numerical results; dashed lines: asymptotes given by Eq. (129).

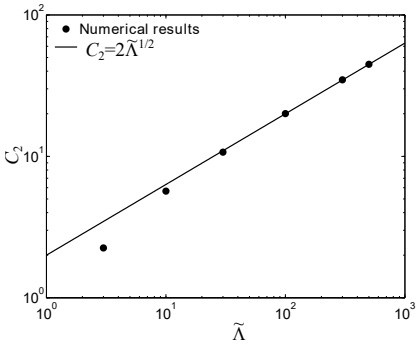

(b) Matching constant C_2 as a function of $\tilde{\Lambda}$.

Fig. 21 Behavior of the interface slope in the intermediate regions: matching of the first and second intermediate regions [12].

3.5 Apparent contact angle

The main result of such a model is the behavior of the interface slope observed at the macroscopic length scale L. According to Eq. (129), the slope depends on the distance x from the CL:

$$\frac{\partial h}{\partial x} \simeq \theta_{micro} - \frac{3\mu D\Delta\rho}{\rho_L \sigma \theta_{micro}^3 \Lambda}\left[\chi\sqrt{\frac{\Lambda}{\ell_K}} + \log\left(\frac{x}{\Lambda}\right)\right]. \tag{131}$$

This expression means that the apparent contact angle that should be obtained as a result of the matching to the macroregion (sec. 2.4.3), logarithmically depends on the macroscopic scale L (i.e. the interfacial curvature radius), similarly to the moving contact line problem.

Suppose that the logarithmic term in Eq. (131) can be neglected. One then obtains an approximate expression of the slope that is independent of the scale L and can thus be associated with the apparent contact angle,

$$\theta_{app} \simeq \theta_{micro} - \frac{3\chi}{\sqrt{\ell_K}} \frac{\mu D}{\rho_L \sigma \theta_{micro}^3} \frac{\Delta\rho}{\sqrt{\Lambda}}. \tag{132}$$

On the other hand, Eq. (132) can also be obtained by tending $\tilde{x} \to \infty$ in Eq. (127), i.e. within the first intermediate region because it is the "in-between" result. In this case one gets instead of $3\chi \simeq 6$ the coefficient $8/\sqrt{\pi C_1} \simeq 6.2$. Two values are very close, which is not surprising because both intermediate regions are matched (in the asymptotic sense) for $\tilde{x} \to \infty$ for the first and $\tilde{x} \to \tilde{\Lambda}$ for the second. The agreement shows simply that the matching has been performed correctly.

Note that Eq. (132) is the result of the intermediate regions where microscopic effects are negligible. Therefore, its form is independent of the microscopic singularity relaxation mechanism. Similarly to the pure vapor case and moving CL, the microscopic details impact only the microregion length scale ℓ_K.

Eq. (132) is very close to the result of Berteloot et al. [5] (one needs to drop the independent Cox-Voinov term in their Eq. (13) since they considered the moving CL case. The boundary layer thickness Λ is included in their parameter J_0. Unlike the approach presented here, Berteloot et al. introduced a microscopic scale phenomenologically, and found the numerical prefactor $3\chi = 8$. In the present approach, the scales are matched rigorously, and a more precise value of $3\chi \simeq 6$ is obtained. Note that Berteloot et al. considered only the first intermediate region $x \ll \Lambda$. The approach described here reveals another logarithmic term that was implicitly neglected by them.

4 Conclusions

While not impacting the contact angles at the nanoscale, evaporation or condensation causes an increase of the apparent (experimentally measurable at the macroscale) contact angle that leads to a change in the wetting properties (both dynamic and static) as if this change were induced by a surface modification. The control of this phenomenon is possible via the control of the local evaporation rate in a tiny vicinity of the contact line via controlling the degree of non-equilibrium of the system. The specific way of control depends on the evaporation regime. Two limiting regimes has

been considered above. Strong evaporation (and, accordingly, a strong change of the wetting properties) can be achieved at evaporation into the atmosphere of pure vapor. It is controlled by the superheating ΔT of the heater with respect to the saturation temperature for the system pressure, like e.g. in boiling. The contact angle depends on many system parameters but the most important dependence is on ΔT and on the equilibrium contact angle (i.e. that at $\Delta T = 0$). Another limiting regime, that of slow evaporation, achieved at isothermal drop drying in the under-saturated atmosphere of a non-condensible gas. It is controlled by the vapor diffusion within the diffusion boundary layer. The main control parameters here are the super-saturation $\Delta\rho$ (with respect to the saturation vapor density for the system temperature), the thickness of the diffusion boundary layer, and of course the equilibrium contact angle.

Because many reasons, it is difficult to measure the contact angles at evaporation conditions. Some of these reasons are the continuous change of the contact angle, the optical aberrations in the presence of thermal gradients, the simultaneous thermal control and optical observations.

It is however possible to predict the contact angles theoretically. The hydrodynamic flow caused by evaporation induce a contact line singularity similar to that caused by the well-studied contact line motion problem. For this reason, the contact angle calculation is a delicate issue and calculation error can be high if the problem is approached incorrectly. Like in the contact line motion problem, several approaches are possible to relax the singularity. At complete wetting, the continuous wetting film approach is possible so the actual triple contact is absent. At much more common case of partial wetting, one can use a model based on the simultaneous action of two effects: the hydrodynamic slip and the kinetic resistance. Another approach consists in the account of the Kelvin effect that is self-sufficient to relax the singularity. The Kelvin effect can be used alone or in any combination with other effects. The models based on the Kelvin effect present an evident advantage of providing the finite values of the evaporation flux and liquid pressure that can be defined a priori and serve as boundary conditions for calculations.

The multi-scale approach is a powerful tool for the accurate and numerically efficient contact angle calculation that is necessary to describe the evaporation (in some cases) for the static and always to describe the contact line motion that is often caused by evaporation. By using the multi-scale approach, one can explicitly define all the parameters (both microscopic and macroscopic) to find the apparent contact angle that is a function of the specific geometry of wetting (drop, bubble, tube, ridge, etc).

5 Acknowledgements

The author would like to express his gratitude to all his coauthors, without whose contribution this work would not be possible. The author would like to thank the European Space Agency for the support through the MAP TOPDESS and CNES for the support in the framework of the GdR MFA.

Nomenclature

ℓ	characteristic length scale [m]
$\mathbf{n}$	normal vector to the interface
A	Hamaker constant [J], area (sec. 1.2.4, sec. 2.4.4) [m^2]
C	arbitrary constant
Ca	capillary number
D	diffusion coefficient of vapor in the non-condensible gas, [m^2/s]
e	Euler number $\simeq 2.71$
f	accommodation coefficient
h	liquid layer thickness [m]
I_n	modified Bessel function of the first kind of the order n
J	mass evaporation flux, [kg/(m^2·s)]
K	curvature, [m^{-1}]
k	heat conductivity [W/(m·K)]
K_n	modified Bessel function of the second kind of the order n
L	macroscopic length scale, [m]
l	length [m]
M	molar mass [kg/mol]
m	mass [kg]
P	surface force energy [J/m^2]
p	pressure [Pa]
q	heat flux [W/m^2]
R	radius of drop base, [m]
r	radial distance, [m]
R^i	interfacial thermal resistance, [(K·m^2)/W]
R^i_{diff}	interfacial kinetic resistance, [s/m]
R_g	universal gas constant [J/(mol·K)]
S	spreading coefficient, [N/m]
T	temperature [K]
t	time [s]
V	volume, [m^3]

v	liquid velocity [m/s]
W	interfacial energy [J/m^2]
w	width of dewetting ridge [m]
x, y, z	cartesian coordinates, [m]
$\mathcal{L}$	latent heat, [J/kg]
$\mathcal{R}$	dimensionless interfacial resistance

Abbreviations

CL	Contact Line

Greek symbols

β	dimensionless slip length
Δ	difference
δ	modified capillary number
γ	Marangoni coefficient, [N/(m·K)]
Λ	thickness of diffusion boundary layer, [m]
μ	liquid shear viscosity, [Pa·s]; chemical potential, [J/kg] (in sec. 1.2.2 only)
ν	liquid kinematic viscosity [m^2/s]
Φ	liquid 1D flux [m^2/s]
ϕ	interface slope
Π	disjoining pressure, [Pa]
ρ	density [kg/m^3]
σ	interface tension [N/m]
θ	contact angle
ε	dimensionless deviation from equilibrium

Superscripts

i	interfacial

Subscripts

ad	adsorption
app	apparent
CL	contact line
K	Kelvin
L	liquid
$micro$	microscopic
S	solid heater or substrate
s	slip
sat	saturation
V	Voinov or vapor

References

[1] Afkhami S, Buongiorno J, Guion A, Popinet S, Saade Y, Scardovelli R, Zaleski S (2018) Transition in a numerical model of contact line dynamics and forced dewetting. J Comput Phys 374:1061 – 1093, DOI 10.1016/j.jcp.2018.06.078

[2] Anderson DM, Davis SH (1994) Local fluid and heat flow near contact lines. J Fluid Mech 268:231 – 265, DOI 10.1017/S0022112094001333

[3] Anderson DM, Janeček V (2018) Comment on L. M. Hocking, "On contact angles in evaporating liquids" [Phys. Fluids 7, 2950–2955 (1995)]. Phys Fluids 30(7):079101, DOI 10.1063/1.5041445

[4] Anderson DM, Cermelli P, Fried E, Gurtin ME, McFadden GB (2007) General dynamical sharp-interface conditions for phase transformations in viscous heat-conducting fluids. J Fluid Mech 581:323 – 370, DOI 10.1017/S0022112007005587

[5] Berteloot G, Pham CT, Daerr A, Lequeux F, Limat L (2008) Evaporation-induced flow near a contact line: Consequences on coating and contact angle. Europhys Lett 83(1):14003, DOI 10.1209/0295-5075/83/14003

[6] Bouzigues CI, Tabeling P, Bocquet L (2008) Nanofluidics in the Debye layer at hydrophilic and hydrophobic surfaces. Phys Rev Lett 101(11):114503, DOI 10.1103/PhysRevLett.101.114503

[7] Brochard-Wyart F, de Meglio JM, Quéré D (1987) Démouillage. Etude du retrait d'un film de liquide non mouillant déposé sur un plan ou une fibre. C R Acad Sci, Ser II 304:553 – 558

[8] Brochard-Wyart F, Di Meglio JM, Quere D, de Gennes PG (1991) Spreading of nonvolatile liquids in a continuum picture. Langmuir 7(2):335 – 338, DOI 10.1021/la00050a023

[9] Carey VP (1992) Liquid-Vapor Phase Change Phenomena. Hemisphere, Washington D.C.

[10] Deegan RD, Bakajin O, Dupont TF, Huber G, Nagel SR, Witten TA (2000) Contact line deposits in an evaporating drop. Phys Rev E 62(1):756 – 765, DOI 10.1103/PhysRevE.62.756

[11] Doumenc F, Guerrier B (2011) A model coupling the liquid and gas phases for a totally wetting evaporative meniscus. Eur Phys J Special Topics 197:281–293, DOI 10.1140/epjst/e2011-01470-7

[12] Doumenc F, Janecek V, Nikolayev VS (2018) Thin wedge evaporation/condensation controlled by the vapor dynamics in the atmosphere. Eur Phys J E 41(12):147, DOI 10.1140/epje/i2018-11758-8

[13] Eggers J (2005) Contact line motion for partially wetting fluids. Phys Rev E 72(6):061605, DOI 10.1103/PhysRevE.72.061605

[14] Eggers J, Pismen LM (2010) Nonlocal description of evaporating drops. Phys Fluids 22(11):112101, DOI 10.1063/1.3491133

[15] Fourgeaud L, Ercolani E, Duplat J, Gully P, Nikolayev VS (2016) Evaporation-driven dewetting of a liquid film. Phys Rev Fluids 1(4):041901, DOI 10.1103/PhysRevFluids.1.041901

[16] Gatapova EY, Graur IA, Kabov OA, Aniskin VM, Filipenko MA, Sharipov F, Tadrist L (2017) The temperature jump at water-air interface during evaporation. Int J Heat Mass Transfer 104:800 – 812, DOI 10.1016/j.ijheatmasstransfer.2016.08.111

[17] de Gennes PG (1985) Wetting: statics and dynamics. Rev Mod Phys 57:827 – 863

[18] Hocking LM (1983) The spreading of a thin drop by gravity and capillarity. Q J Mechanics Appl Math 36(1):55 – 69, DOI 10.1093/qjmam/36.1.55

[19] Hocking LM (1995) On contact angles in evaporating liquids. Phys Fluids 7:2950 – 2955, DOI 10.1063/1.868672

[20] Hu H, Larson R (2002) Evaporation of a sessile droplet on a substrate. J Phys Chem B 106(6):1334 – 1344, DOI 10.1021/jp0118322

[21] Huang DM, Sendner C, Horinek D, Netz RR, Bocquet L (2008) Water slippage versus contact angle: A quasiuniversal relationship. Phys Rev Lett 101(22):226101, DOI 10.1103/PhysRevLett.101.226101

[22] Israelachvili JN (1992) Intermolecular and Surface Forces, 2nd edn. Academic Press, London

[23] Janeček V (2012) Evaporation at microscopic scale and at high heat flux. PhD thesis, Université Pierre et Marie Curie Paris 6, URL `http://tel.archives-ouvertes.fr/tel-00782517`

[24] Janeček V, Anderson DM (2016) Microregion model of a contact line including evaporation, kinetics and slip length. Interfacial Phenomena and Heat Transfer 4(2-3):93 – 107, DOI 10.1615/InterfacPhenomHeatTransfer.2017017202

[25] Janeček V, Nikolayev VS (2012) Contact line singularity at partial wetting during evaporation driven by substrate heating. Europhys Lett 100(1):14003, DOI 10.1209/0295-5075/100/14003

[26] Janeček V, Nikolayev VS (2013) Apparent-contact-angle model at partial wetting and evaporation: impact of surface forces. Phys Rev E 87(1):012404, DOI 10.1103/PhysRevE.87.012404

[27] Janeček V, Nikolayev VS (2014) Triggering the boiling crisis: a study of the dry spot spreading mechanism. Interfacial Phenom Heat Transf 2(4):363 – 383, DOI 10.1615/InterfacPhenomHeatTransfer.2015012273

[28] Janeček V, Andreotti B, Pražák D, Bárta T, Nikolayev VS (2013) Moving contact line of a volatile fluid. Phys Rev E 88(6):060404, DOI 10.1103/PhysRevE.88.060404

[29] Janeček VV, Doumenc F, Guerrier B, Nikolayev VS (2015) Can hydrodynamic contact line paradox be solved by evaporation-condensation? J Colloid Interface Sci 460:329 – 338, DOI 10.1016/j.jcis.2015.08.062

[30] Koplik J, Banavar JR (1995) Continuum deductions from molecular hydrodynamics. Annu Rev Fluid Mech 27:257 – 292, DOI 10.1146/annurev.fl.27.010195.001353

[31] Landau LD, Lifshitz EM (1980) Statistical physics. Pergamon Press, Oxford

[32] Lauga E, Brenner MP, Stone HA (2007) Microfluidics: The no-slip boundary condition. In: Tropea C, Yarin A, Foss J (eds) Springer Handbook of Experi-

mental Fluid Dynamics, Springer, New York, chap 19, pp 1217 – 1240, DOI 10.1007/978-3-540-30299-5_19, https://arxiv.org/pdf/cond-mat/0501557.pdf

[33] Marek R, Straub J (2001) The origin of thermocapillary convection in subcooled nucleate pool boiling. Int J Heat Mass Transfer 44:619 – 632, DOI 10.1016/S0017-9310(00)00124-1

[34] Moosman S, Homsy GM (1980) Evaporating menisci of wetting fluids. J Colloid Interface Sci 73(1):212 – 223, DOI 10.1016/0021-9797(80)90138-1

[35] Morris SJS (2001) Contact angles for evaporating liquids predicted and compared with existing experiments. J Fluid Mech 432:1 – 30, DOI 10.1017/S0022112000003074

[36] Morris SJS (2014) On the contact region of a diffusion-limited evaporating drop: a local analysis. J Fluid Mech 739:308 – 337, DOI 10.1017/jfm.2013.577

[37] Nikolayev VS (2010) Dynamics of the triple contact line on a nonisothermal heater at partial wetting. Phys Fluids 22(8):082105, DOI 10.1063/1.3483558

[38] Nikolayev VS, Beysens DA (1999) Boiling crisis and non-equilibrium drying transition. Europhys Lett 47(3):345 – 351, DOI 10.1209/epl/i1999-00395-x

[39] Nikolayev VS, Chatain D, Garrabos Y, Beysens D (2006) Experimental evidence of the vapor recoil mechanism in the boiling crisis. Phys Rev Lett 97:184503, DOI 10.1103/PhysRevLett.97.184503

[40] Petroff NP (1883) Friction in machines and the effect of lubricant. Inzhenernyj Zhurnal, Sankt-Peterburg 1-4:71 – 140, 228 – 279, 377 – 436 and 535 – 564, published in four issues, in Russian

[41] Pham CT, Berteloot G, Lequeux F, Limat L (2010) Dynamics of complete wetting liquid under evaporation. Europhys Lett 92(5):54005, DOI 10.1209/0295-5075/92/54005

[42] Pismen LM, Eggers J (2008) Solvability condition for the moving contact line. Phys Rev E 78(5):056304, DOI 10.1103/PhysRevE.78.056304

[43] Pit R, Hervet H, Léger L (2000) Direct experimental evidence of slip in hexadecane: solid interfaces. Phys Rev Lett 85:980 – 983, DOI 10.1103/PhysRevLett.85.980

[44] Pomeau Y (2000) Representation of the moving contact line in the equations of fluid mechanics. C R Acad Sci, Ser IIb 238:411 – 416, DOI 10.1016/S1620-7742(00)00043-X, (in French)

[45] Potash M, Wayner PC (1972) Evaporation from a two-dimensional extended meniscus. Int J Heat Mass Transfer 15(10):1851 – 1863, DOI 10.1016/0017-9310(72)90058-0

[46] Poulard C, Guéna G, Cazabat AM, Boudaoud A, Ben Amar M (2005) Rescaling the dynamics of evaporating drops. Langmuir 21(18):8226 – 8233, DOI 10.1021/la050406v

[47] Raj R, Kunkelmann C, Stephan P, Plawsky J, Kim J (2012) Contact line behavior for a highly wetting fluid under superheated conditions. Int J Heat Mass Transfer 55(9-10):2664 – 2675, DOI 10.1016/j.ijheatmasstransfer.2011.12.026

[48] Rednikov AY, Colinet P (2011) Truncated versus extended microfilms at a vapor-liquid contact line on a heated substrate. Langmuir 27(5):1758 – 1769, DOI 10.1021/la102065c

[49] Reyes R, Wayner PC Jr (1996) A Kelvin–Clapeyron adsorption model for spreading on a heated plate. J Heat Transfer 118(4):822 – 830, DOI 10.1115/1.2822576

[50] Reynolds O (1886) On the theory of lubrication and its application to Mr Beauchamp Tower's experiments, including an experimental determination of viscosity of olive oil. Phil Trans R Soc Lond 177:157 – 234, DOI 10.1098/rstl.1886.0005

[51] Snoeijer JH, Andreotti B (2008) A microscopic view on contact angle selection. Phys Fluids 20(5):057101, DOI 10.1063/1.2913675

[52] Snoeijer JH, Andreotti B (2013) Moving contact lines: Scales, regimes, and dynamical transitions. Annu Rev Fluid Mech 45(1):269 – 292, DOI 10.1146/annurev-fluid-011212-140734

[53] Snoeijer JH, Eggers J (2010) Asymptotic analysis of the dewetting rim. Phys Rev E 82(5):056314, DOI 10.1103/PhysRevE.82.056314

[54] Stephan P, Hammer J (1994) A new model for nucleate boiling heat transfer. Heat Mass Transfer 30(2):119 – 125, DOI 10.1007/BF00715018

[55] Sui Y, Ding H, Spelt PD (2014) Numerical simulations of flows with moving contact lines. Annu Rev Fluid Mech 46(1):97 – 119, DOI 10.1146/annurev-fluid-010313-141338

[56] Tsoumpas Y, Dehaeck S, Galvagno M, Rednikov A, Ottevaere H, Thiele U, Colinet P (2014) Nonequilibrium Gibbs criterion for completely wetting volatile liquids. Langmuir 30(40):11847 – 11852, DOI 10.1021/la502708f

[57] Voinov O (1976) Hydrodynamics of wetting. Fluid Dyn 11(5):714 – 721, DOI 10.1007/BF01012963

[58] Wayner PC, Kao YK, LaCroix LV (1976) The interline heat-transfer coefficient of an evaporating wetting film. Int J Heat Mass Transfer 19:487 – 492, DOI 10.1016/0017-9310(76)90161-7

[59] Yeh EK, Newman J, Radke CJ (1999) Equilibrium configurations of liquid droplets on solid surfaces under the influence of thin-film forces: Part I. Thermodynamics. Colloids Surf, A 156(1-3):137 – 144, DOI 10.1016/S0927-7757(99)00065-5

[60] Yeh EK, Newman J, Radke CJ (1999) Equilibrium configurations of liquid droplets on solid surfaces under the influence of thin-film forces: Part II. Shape calculations. Colloids Surf, A 156(1-3):525 – 546, DOI 10.1016/S0927-7757(99)00110-7